

Variable UV Absorption in the Seyfert 1 Galaxy NGC 3516: The Case for Associated UV and X-ray Absorption¹

S. B. Kraemer², D. M. Crenshaw³, I.M. George^{4,5}, H. Netzer⁶, T.J. Turner^{4,5}, & J.R. Gabel²

Received _____; accepted _____

submitted to *The Astrophysical Journal*

¹Based on observations made with the NASA/ESA Hubble Space Telescope. STScI is operated by the Association of Universities for Research in Astronomy, Inc. under the NASA contract NAS5-26555.

²Catholic University of America, and Laboratory for Astronomy and Solar Physics, NASA's Goddard Space Flight Center, Code 681, Greenbelt, MD 20771; stiskraemer@yancey.gsfc.nasa.gov.

³Department of Physics and Astronomy, Georgia State University, Atlanta, GA 30303.

⁴Joint Center for Astrophysics, Physics Dept., University of Maryland Baltimore County, 1000 Hilltop Circle, Baltimore, MD 21250

⁵Laboratory for High Energy Astrophysics, NASA's Goddard Space Flight Center, Code 662 Greenbelt, MD 20771.

⁶School of Physics and Astronomy, Raymond and Beverly Sackler Faculty of Exact Sciences, Tel-Aviv University, Tel-Aviv 69978, Israel.

ABSTRACT

We present observations of the UV absorption lines in the Seyfert 1 galaxy NGC 3516, obtained at a resolution of $\lambda/\Delta\lambda \approx 40,000$ with the Space Telescope Imaging Spectrograph (STIS) on 2000 October 1. The UV continuum was ~ 4 times lower than that observed during 1995 with the Goddard High Resolution Spectrograph (GHRS), and the X-ray flux from a contemporaneous *Chandra X-ray Observatory (CXO)* observation was a factor of ~ 8 below that observed with *ASCA*. The STIS spectra show kinematic components of absorption in Ly α , C IV, and N V at radial velocities of -376 , -183 , and -36 km s $^{-1}$ (components 1, 2, and 3+4, respectively), which were detected in the earlier GHRS spectra; the last of these is a blend of two GHRS components that have increased greatly in column density. Four additional absorption components have appeared in the STIS spectra at radial velocities of -692 , -837 , -994 , and -1372 km s $^{-1}$ (components 5 through 8); these may also have been present in earlier low-flux states observed by the *International Ultraviolet Explorer (IUE)*. Based on photoionization models, we suggest that the components are arranged in increasing radial distance in the order, 3+4, 2, 1, followed by components 5 – 8. We have achieved an acceptable fit to the X-ray data using the combined X-ray opacity of the UV components 1, 2 and 3+4. By increasing the UV and X-ray fluxes of these models to match the previous high states, we are able to match the GHRS C IV column densities, absence of detectable C IV absorption in components 5 through 8, and the 1994 *ASCA* spectrum. We conclude that variability of the UV and X-ray absorption in NGC 3516 is primarily due to changes in the ionizing flux.

Subject headings: galaxies: Seyfert - X-rays: galaxies - ultraviolet: galaxies -

galaxies: individual (NGC 3516)

1. Introduction

It is now understood that intrinsic absorption is a common phenomenon in Seyfert 1 galaxies, present in more than half of those observed with the spectrographs aboard the *Hubble Space Telescope (HST)* (Crenshaw et al. 1999). Among those Seyferts that show absorption, high ionization resonance lines such as N V $\lambda\lambda 1238.8, 1242.8$ and C IV $\lambda\lambda 1548.2, 1550.8$ are always present, along with Ly α , while lower ionization lines, such as Si IV $\lambda\lambda 1393.8, 1402.8$, and Mg II $\lambda\lambda 2796.3, 2803.5$, are less common. The absorption lines can be blueshifted (by up to 2100 km s^{-1}) with respect to the systemic velocities of the host galaxies, indicating net radial outflow. However, UV absorption lines can arise in dusty gas within the plane of the host galaxy (Crenshaw et al. 2001; Crenshaw et al. 2002); these are often saturated and at velocities close to systemic. The ionic columns can be highly variable, which may be the result of changes in response to the ionizing continuum, as first suggested in case of NGC 4151 by Bromage et al. (1985) and Espey et al. (1998), and discussed in detail in Crenshaw et al. (2000a) and Kraemer et al. (2001a), or transverse motion, as appears to be the case for NGC 5548 and NGC 3783 (Crenshaw & Kraemer 1999; Kraemer, Crenshaw, & Gabel 2001b). In fact, both mechanisms may be at work in individual AGN. In either case, the variability is indicative of the proximity of the absorbers to the central active nucleus of these galaxies; in the case of NGC 4151, constraints on the density and ionization of the strongest absorption system place it within 0.03 pc of the continuum source (Kraemer et al. 2001a).

The presence of intrinsic absorption, typically in the form of bound-free edges of O VII and O VIII, has been detected in the X-ray spectra of a similar fraction of Seyfert 1 galaxies (Reynolds 1997; George et al. 1998). Most recently, spectra obtained with the *Chandra X-ray Observatory (CXO)* have revealed that X-ray absorption lines associated with this material are also blue-shifted (Kaastra et al. 2000; Kaspi et al. 2000, Collinge et al. 2001).

The connection between the X-ray and UV absorption is complex and there is likely a range of physical conditions within the absorbers (see Kriss et al. 1996a; Kriss et al. 2000; Krolik & Kriss 2001). Furthermore, there is evidence that the X-ray absorbers in some sources must also be multi-zoned (Otani et al. 1996; Reynolds et al. 1997).

NGC 3516 ($z = 0.00875$) is one of the few Seyfert 1 galaxies with UV absorption lines, specifically N V, C IV, and Si IV, strong enough to have been detected with the *International Ultraviolet Explorer (IUE)* (Ulrich & Boisson 1983). These lines are known to vary on timescales as short as weeks (Voit, Shull, & Begelman 1987; Walter et al. 1990; Kolman, Halpern, & Martin 1993). Walter et al. suggested that the C IV absorption consists of a narrow, apparently stable component in the core of the broad emission lines and a variable, broad, blue-shifted component. Koratkar et al. (1996) found the blueshifted component present in *IUE* spectra in 1978, but it had disappeared between 1989 and 1993, and has been absent in subsequent *Hopkins Ultraviolet Telescope (HUT)* (Kriss et al. 1996b) and *HST/Goddard High Resolution Spectrograph (GHRS)* (Crenshaw, Maran, & Mushotzky 1998) observations. Based on GHRS spectra, Crenshaw et al. (1998) determined that the absorption in the core of the line (Walter et al.’s “stable” component) consisted of two broad components, with velocities of -380 and -150 km s $^{-1}$, and two narrow components at -90 and -30 km s $^{-1}$.

NGC 3516 also exhibits strong, variable X-ray absorption (Kolman et al. 1993; Nandra & Pounds 1994; Kriss et al. 1996a; Mathur, Wilkes, & Aldcroft 1997). Although Mathur et al. (1997) suggested that the X-ray and UV absorption arises in gas characterized by a single set of physical conditions, Kriss et al. (1996a) modeled the X-ray absorber as two zones, one with an ionization parameter (the ratio of the density of photons with energies ≥ 13.6 eV to the number density of hydrogen atoms at the illuminated face of the zone) $U = 1.66$ and a total hydrogen column density of 1.4×10^{22} cm $^{-2}$ and a lower ionization

zone with $U = 0.32$ and a total column density of $6.9 \times 10^{21} \text{ cm}^{-2}$, and argued that not all of the UV lines could form in these zones. In our previous paper (Netzer et al. 2002; hereafter Paper I), we presented an analysis of the *CXO*/Low Energy Transmission Grating Spectrograph (LETGS) spectrum obtained on 2000 October 6. The X-ray continuum flux, $\text{Flux}_{6.4\text{KeV}} = (1.6 \pm 0.2) \times 10^{-4} \text{ photons cm}^{-2} \text{ s}^{-1} \text{ KeV}^{-1}$, was close to its historic minimum, roughly a factor of 8 – 10 below maximum (observed in 1994 with *ASCA*). We found that the variations in observed flux and spectra at these epochs is consistent with an absorber of constant column density ($7.9 \times 10^{21} \text{ cm}^{-2}$) whose ionization state has changed in response to the variation in the ionizing continuum, specifically: for the current low flux state, $U = 0.19$, while it would be a factor of 8 to 10 higher in the high flux state (depending on the amplitude of the UV continuum variations), in rough agreement with the high ionization component described by Kriss et al. (1996a). The model predicts large column densities ($\sim 10^{17} \text{ cm}^{-2}$) for N V and C IV, hence one or more of the observed kinematic components of the UV absorption should be associated with the X-ray absorber.

We obtained echelle spectra of NGC 3516 with the Space Telescope Imaging Spectrograph (STIS) on HST under a STIS Guaranteed Time Observer Program. In this paper, we present our analysis of the physical conditions in the UV absorbers, nature of their variability, and the connection to the X-ray absorption detected in our contemporaneous *CXO*/LETGS observation.

2. Observations and Data Analysis

2.1. New STIS and Previous GHRS Observations

We obtained STIS echelle spectra of the nucleus of NGC 3516 through a $0''.2 \times 0''.2$ aperture on 2000 October 1. These observations and two previous observations of the C IV

region with the Goddard High Resolution Spectrograph (GHRS) are detailed in Table 1. The reduction of the GHRS spectra is described in Crenshaw et al. (1998, 1999). We reduced the STIS echelle spectra using the IDL software developed at NASA’s Goddard Space Flight Center for the STIS Instrument Definition Team. The data reduction includes a procedure to remove the background light from each order using a scattered light model devised by Lindler (1999). The individual orders in each echelle spectrum were spliced together in the regions of overlap.

Figure 1 compares the C IV regions from the high-resolution spectra obtained at the three epochs. As noted in Crenshaw et al. (1998, 1999), the GHRS observations in 1995 showed four kinematic components of absorption in C IV (which we will refer to as the “core components”). Although there was a decrease in the underlying continuum plus broad C IV emission over the six-month interval in 1995, there was no evidence for a change in the ionic column density (or radial velocity coverage) of any component. The new STIS observations in 2000 October show a further decrease in the continuum plus broad C IV emission, plus a dramatic change in some of the C IV absorption components. In the STIS spectrum, there is a strong absorption feature at the position of the weak GHRS components 3 and 4. In addition, there is significant new absorption in the blue wing of the broad C IV profile, in the 1553 – 1559 Å region. This new absorption is reminiscent of the broad, variable blueshifted absorption seen in the C IV profile from early *IUE* observations (Koratkar et al. 1996), which will be discussed later in this section. There is no evidence for significant changes in components 1 and 2, which are heavily saturated at all three epochs.

Figure 2 shows portions of the STIS E140M spectra where intrinsic absorption is detected in other ions. Fluxes are plotted as a function of the radial velocity (of the strongest member, for doublets), relative to the systemic redshift of $z = 0.00875$ from the optical emission lines (Crenshaw et al. 1999), since H I 21-cm measurements are

not available. Each of the original 4 absorption components are present in Ly α and the doublets of N V $\lambda\lambda$ 1238.8, 1242.2 and C IV λ 1548.2, 1550.8. In addition, Si IV $\lambda\lambda$ 1393.8, 1402.8 absorption is present in components 1 and 2. We have also detected C II λ 1334.5, C II* λ 1335.7 (fine-structure line), and Mg II $\lambda\lambda$ 2796.3, 2803.5 intrinsic absorption, all in component 1 only. We have not reliably detected any other intrinsic absorption line in the E140M or E230M spectra.

We have separated the new blueshifted absorption into four distinct kinematic components (5 – 8; which we will refer to as the “blueshifted components”). Our criteria for identification of a component are that it must be distinct in radial velocity space (i.e., not severely blended with other components), and clearly present in N V or C IV. Component 5 is by far the strongest and broadest new component, whereas components 6 – 8 are relatively weak.

2.2. Measurements and Observational Results

The procedures we used to measure the intrinsic absorption lines follow those of Crenshaw et al. (1999). To determine the shape of the underlying emission, we fit a cubic spline to regions on either side of the absorption, and then normalized the absorption profiles by dividing the observed spectra by the spline fits. We determined the covering factor C_{los} , which is the fraction of continuum plus emission that is occulted by the absorber in our line of sight, using the technique of Hamann et al. (1997) for doublets. We have relied on the C IV doublets to determine these values, since many of the N V doublets are contaminated by Galactic absorption or blending of kinematic components. Due to the modest signal-to-noise of the spectra and blending of components in the wings, C_{los} can only be determined reliably in the cores of the lines. We are not able to accurately deconvolve components 3 and 4 in the STIS spectra (see Figure 2), so they are treated as

one component (3+4) in this paper.

Table 2 gives the radial velocity centroids, widths (FWHM), covering factors, and associated one-sigma errors for each kinematic component. These velocity centroids represent the means and standard deviations determined from the measurements of the C IV, N V, Si IV, and Ly α profiles (when available for the latter two). Compared to the GHRIS measurements (Crenshaw et al. 1999), there is no evidence for a change in the radial velocities of components 1 – 4, except for perhaps a slight shift in component 2 from -148 km s $^{-1}$ (GHRIS) to -183 km s $^{-1}$ (possibly due to increased absorption in the blue wing of this component). The radial velocity centroid of component 3+4 is very close to the position of the GHRIS value for component 4, suggesting (but not proving) that component 4 may be the one responsible for the large increase in absorption. Our original suggestion that components 3 and 4 may be due to the interstellar medium or halo of the host galaxy (Crenshaw et al. 1998) is therefore still a possible explanation for one of these components (probably component 3), but not the other (our models are based on the assumption that these components are essentially co-located, near the ionizing source).

To determine the FWHM of the components, we used values from relatively unsaturated lines, to get an indication of the true velocity spread for each component. Thus, we used the STIS Si IV lines for components 1 and 2, the GHRIS C IV lines for components 3 and 4, and the STIS Ly α , N V, and C IV lines for components 5 – 8. For components 1 and 2, the FWHMs are therefore smaller than those measured from the GHRIS C IV profiles (Crenshaw et al. 1999), since the latter are heavily saturated.

Next, we examine the covering factors in Table 2. The covering factors for components 1 and 2 are *consistent* with a value of one, although we cannot rule out the possibility that they are as small as 0.96. Component 3+4 shows the strongest evidence for a non-unity covering factor. Although the aperture for the STIS observations is small, there is likely

to be some emission from the narrow-line region (NLR) that is unocculted (see Kraemer et al. 2001; Brotherton et al. 2002). This could explain the nonunity covering factor for component 3+4 since it is near the systemic redshift, where the NLR contribution is strongest. To illustrate this point, we have simulated the NLR contribution by reproducing Gaussians at the systemic velocity in Figure 2. We kept the doublet ratios fixed at 2:1, chose a single value for the FWHM ($= 165 \text{ km s}^{-1}$) that provided a good overall fit, and scaled the intensities to obtain the best fit for each ion. Given our assumptions, the NLR emission provides a reasonably accurate match to the troughs of the saturated lines (note the contamination of N V $\lambda 1242.8$ by Galactic S II). The error in covering factor for component 5 is too large to make a definite conclusion. We could not determine reliable values for components 6 – 8, since the profiles are shallow and relatively noisy. Lower limits from $L\alpha$ and estimates from N V are consistent with the covering factors determined from C IV.

To determine the ionic column densities, we converted each normalized profile to optical depth as a function of radial velocity, and integrated across the profile, as described in Crenshaw et al. (1999). For components 1 and 2, the Si IV profiles are much narrower than the profiles of $L\alpha$, N V, and C IV, suggesting that the latter are heavily saturated (assuming the same intrinsic velocity dispersion for all ions). By the same token, components 3 and 4 in the GHRS spectra are narrow in C IV compared to the STIS component 3+4, again suggesting heavy saturation in the latter. Furthermore, the possibility of nonunity covering factors for components 1, 2, and 3+4 suggests that the column densities may be much larger than would be determined for $C_{los} = 1$. Thus, we can only determine lower limits to the column densities for these lines (by assuming $C_{los} = 1$), and the column densities for components 1 and 2 from the GHRS spectra (Crenshaw et al. 1998, 1999) should be taken as lower limits. For component 5, even if $C_{los} = 0.6$, the depth of the lines are such that they are not heavily saturated. As we mentioned previously, we

do not have reliable measurements of C_{los} for components 6 – 8. Since these components are shallow, they are unlikely to be saturated (including Ly α in these components), unless the covering factors are extremely small, which seems unlikely. Thus, we have assumed $C_{los} = 1$ for components 5 – 8.

Table 3 gives our measurements of STIS and GHRS column densities for all lines that have been detected in at least one component. We include lower limits for heavily saturated lines and upper limits for undetected lines to constrain the photoionization models.

2.3. Comparison with Previous Low-Resolution Spectra

To pursue a possible connection between the continuum flux and the strength of the C IV absorption, we have examined all of the far-UV spectra that have been obtained of NGC 3516. Table 4 lists the additional far-UV spectra (i.e., those not listed in Table 1), which were obtained at lower spectral resolutions by the *IUE*, *HUT*, and the Faint Object Spectrograph (FOS) and Space Telescope Imaging Spectrograph (STIS) on *HST*. We have retrieved the most recently processed versions of these spectra from the *IUE* and *HST* archives in order to measure their continuum fluxes and examine their C IV profiles. For the *HUT* spectrum, we determined the continuum flux directly from the plot in Kriss et al. (1996b).

We measured the continuum fluxes by averaging the points in a bin centered at 1460 Å (observed frame) with a width of 20 Å. We determined the one-sigma flux errors from the standard deviations of the averages; for the *IUE* spectra, this technique is known to overestimate the errors (Clavel et al. 1991), and we scaled the errors for these observations by a factor of 0.7 to ensure that observations taken on the same day agreed to within the errors (on average). For the two GHRS spectra, the continuum regions adjacent to

the broad C IV emission profile were not observed. In this case, we used separate fits to the continuum and broad emission in the STIS C IV region and tried different linear combinations of these fits until an accurate match was obtained to the continuum plus broad emission in each GHRS spectrum.

Figure 3 shows that the far-UV continuum of NGC 3516 has varied dramatically over a span of 22 years. Early *IUE* observations were obtained when NGC 3516 was in low to moderate states, whereas later observations, including the intensive monitoring campaign of 1996 (\sim JD 2,490,000, see Koratkar et al. 1996), were obtained primarily at a high state. The last *IUE* observations and subsequent observations by other instruments demonstrate the rapid variability of NGC 3516; in particular, the FOS observations show a factor of 5 variation (ratio of brightest to faintest) over the course of 11 months (see Goad et al. 1999). However, the trend is to lower flux levels in the most recent observations. The new STIS observations were obtained at very low (but not unprecedented) continuum flux levels.

To examine the previous behavior of the C IV profile as a function of continuum luminosity, we have placed the *IUE* spectra into three categories based on their continuum fluxes at 1460 Å: low ($0 - 2.0 \times 10^{-14}$ ergs s $^{-1}$ cm $^{-2}$ Å $^{-1}$), medium ($2.0 - 4.0 \times 10^{-14}$ ergs s $^{-1}$ cm $^{-2}$ Å $^{-1}$), and high ($4.0 - 7.0 \times 10^{-14}$ ergs s $^{-1}$ cm $^{-2}$ Å $^{-1}$). We averaged the spectra (weighting by exposure time) in each category. Figure 4 shows the average spectra in the C IV profiles. For comparison, we binned the GHRS and STIS spectra to the same wavelength sampling as the *IUE* spectra (1.67 Å per bin), and smoothed slightly to match the *IUE* resolution (6 Å FWHM). We overplot the binned high-state GHRS and low-state STIS spectra in Figure 4.

The *IUE* spectra in Figure 4 show a remarkable change in the C IV profile as a function of continuum luminosity. The blue emission peak just shortward (in wavelength) of the central absorption feature is stronger than the red peak at high luminosity, but becomes

weaker and shifts to shorter wavelength at lower luminosities. The binned GHRS and STIS spectra show the same effect. Comparison with Figure 1 shows that this effect is due to increased absorption from components 5 – 8 in the low-state STIS spectrum. This effect has been noticed in previous *IUE* studies. Walter et al. (1990) characterized the C IV absorption in *IUE* spectra as a blend of a narrow stable component in the core of the emission line plus a variable broad and blueshifted component. The similar appearances of the low-state *IUE* and STIS C IV profiles indicate that the variable blue-shifted absorption covers a similar range in radial velocity, and *suggest* that they originate from the same kinematic components. This would not be too surprising, since long-term stability in the radial velocities of absorption components is a common trait in Seyfert 1 galaxies (Crenshaw et al. 1999).

Koratkar et al. (1996) showed that the blueshifted component disappeared in *IUE* spectra between 1989 October and 1993 February (when NGC 3516 was in a high state). At the time, it was not clear if this effect was due to evolution of the absorbers (e.g., bulk motion of gas out of the line of sight) or to a change in the ionization of the gas (e.g., a decrease in the C IV column due to an increase in the ionizing continuum, coincident with the increase in the UV continuum). There are several pieces of evidence that indicate that the latter (variable ionization) is certainly an important, and probably dominant, contributor to the C IV absorption variability. 1) Our examination of individual *IUE* spectra indicate that the C IV profile variability is more correlated with continuum flux than with time. In particular, the moderately high states at early times and the moderately low states at the end of the *IUE* observations confirm the above trend. 2) Walter et al. (1990) found an anticorrelation between continuum flux and C IV equivalent width in the *IUE* spectra, consistent with this scenario. 3) The individual FOS observations, which span a large range (factor of 5) in continuum flux, show the same effect of decreasing blue peak with decreasing flux (see the spectra in Goad et al. 1999). 4) The high resolution STIS and

GHRSS spectra confirm this effect, and identify the kinematic components responsible for the change in the C IV profile. We note that the same effect has been seen in the intrinsic O VI absorption in NGC 3516 (Hutchings et al. 2001): high-velocity absorption (consistent with components 5 – 8) appeared in a low-state *FUSE* observation, but was not apparent in a moderately high-state *HUT* observation obtained five years earlier. Thus, we believe we have strong evidence for variable ionization of the absorption in NGC 3516, such that the high-velocity UV absorption disappears at high continuum fluxes.

3. Photoionization Models

3.1. Inputs to the Models

Photoionization models for this study were generated using the code CLOUDY90 (Ferland et al. 1998). We have modeled the absorbers as matter-bounded slabs of atomic gas, irradiated by the ionizing continuum radiation emitted by the central source. As per convention, the models are parameterized in terms of the ionization parameter, U . Each separate kinematic component was initially modeled with one set of initial conditions, i.e., U , n_H , and the total hydrogen column density, $N_H (= N_{H I} + N_{H II})$ ⁷. For the models, we have assumed only thermal broadening, since 1) the absorption line widths could be due to the superposition of unresolved kinematic components and 2) comparison models assuming turbulent velocities of $\leq 300 \text{ km s}^{-1}$ predict nearly identical ionic columns. Since the strongest absorption lines in components 1, 2, and 3+4 ($\text{Ly}\alpha$, N V, and C IV) are saturated, we can only compare the model predictions to lower limits for the ionic column densities. However, the predictions for these components are constrained by the upper

⁷We use N_{XM} to denote the ionic column density, where “X” is the atomic symbol and “M” is the ionization state.

limits, or relatively small column densities, derived for lower ionization species, such as C II and Mg II. Furthermore, total X-ray opacity predicted by the UV absorbers models cannot exceed that which we determined from the *CXO*/LETGS spectrum (Paper I).

In Paper I, we suggested that the total reddening in NGC 3516 may be slightly higher than $E_{B-V} = 0.06$ (determined by Kriss et al. [1996b]). First, using combined STIS and FOS data from similar flux states, we dereddened the continuum using the Galactic curve (Savage & Mathis 1979) until we matched the NGC 4151 continuum. With the caveat that the NGC 3516 spectrum is from a low state, hence the FUV could be intrinsically depressed (Clavel et al. 1991; Crenshaw et al. 1996), while the NGC 4151 spectrum is from a moderately high state, we derived an upper limit of $E_{B-V} \leq 0.15$. Alternately, we found, using the average continuum fluxes at 1460\AA and 5510\AA determined by Edelson et al. (2000) during their STIS monitoring campaign that an underlying continuum of the form $F_\nu \propto \nu^\alpha$, where $\alpha = -1$, is consistent with an $E_{B-V} \approx 0.10$. Therefore, we have adopted a reddening value of $E_{B-V} = 0.10 \pm 0.05$, of which 0.04 is Galactic (Schlegel, Finkbeiner, & Davis 1998). This is in rough agreement with Kriss et al. (1996b), but suggests an UV power-law that is more consistent with typical values for low luminosity AGN (Wills et al. 1985). If the dust composition and dust-to-gas ratio are the same as in our Galaxy (see Mathis, Rumpl, & Nordsieck 1977), the intrinsic reddening, $E_{B-V} \approx 0.06$, requires a neutral hydrogen column of $\sim 3.0 \times 10^{20} \text{ cm}^{-2}$ (Shull & van Steenberg 1985). Note, however, that the gas within which the dust resides need not be neutral (see Brandt, Fabian, & Pounds 1996), nor might we expect that the dust near an AGN is the same as that found in the Galactic ISM (Pitman, Clayton, & Gordon 2000; Kraemer et al. 2000; Crenshaw et al. 2002).

As in Paper I, we have assumed that the UV power-law continuum extends out into the EUV, at which point it must steepen to meet the low-energy extension of the X-ray

continuum. Hence, we have approximated the spectral energy distribution (SED), as a power-law, with the following indices: $\alpha = -1$ below 100 eV, $\alpha = -2.3$ over the range $100 \text{ eV} \leq h\nu < 500 \text{ eV}$, and $\alpha = -0.7$ above 500 eV. Assuming $H_0 = 75 \text{ ks s}^{-1} \text{ Mpc}^{-1}$, the total Lyman continuum photon luminosity is $Q \approx 2 \times 10^{53} \text{ photons sec}^{-1}$, roughly twice that for NGC 4151 when it was in a recent low luminosity state (Kraemer et al. 2001a). It should be noted that the power-law break could occur at lower energies, in which case the ratio of the X-ray ionization parameter (see George et al. 1998) to U would be somewhat larger, and the relative fractions of highly ionized species, such as O VII and O VIII, would be somewhat higher than our predictions. We have also modeled the UV absorbers in the 1995 high state observed with the GHRS. In addition to a higher overall ionizing luminosity, we have assumed a slightly different SED, as discussed in Section 4.3.

We have assumed roughly solar element abundances (cf. Grevesse & Anders 1989), which are, by number relative to H, as follows: He = 0.1, C = 3.4×10^{-4} , N = 1.2×10^{-4} , O = 6.8×10^{-4} , Ne = 1.1×10^{-4} , Mg = 3.3×10^{-5} , Si = 3.1×10^{-5} , S = 1.5×10^{-5} , and Fe = 4.0×10^{-5} . The absorbing gas is assumed to be free of cosmic dust.

3.2. Relative Distances of the Absorbers

As discussed in Section 2, the covering factor for each of the core components of absorption is > 0.9 . Hence, the simplest geometric arrangement has the absorbers separated in radial position from the central source, but subtending the same solid angle, i.e., “screening” each other from the ionizing continuum. As a result, the ionizing continuum that reaches the absorbers is diluted by the inverse square of its distance and filtered by intervening gas. This arrangement has important consequences for the response of the screened absorbers to changes in the luminosity of the central source, since they are affected by both changes in the ionizing flux *and* the opacity of the intervening gas.

The core components were present in C IV in GHRs spectra taken while the continuum flux of NGC 3516 was ≥ 4 times higher than during our STIS observations, and components 1 and 2 were highly saturated (Crenshaw et al. 1998). In the STIS spectra each of the core components possesses saturated Ly α , N V, and C IV lines. Component 1 has saturated Si IV and lines from several low ionization species, hence must be the most optically thick at the He II Lyman limit. Based on our photoionization models, the most dramatic changes in the transmitted ionizing continuum occur when there is a large drop in the He II opacity, to the extent that a screened component which possessed a C IV column of $> 10^{15} \text{ cm}^{-2}$ (e.g., a model with $N_H = 10^{21} \text{ cm}^{-2}$ and a low-state ionization parameter $U = 0.1$), would have essentially all of its carbon ionized out of C IV during the high state. Since each of these absorbers was present while NGC 3516 was in a high flux state, it is unlikely that component 1 is closest to the ionizing source. Expanding on this, we found that the best fit to the observed ionic columns is achieved when the three components are arranged in increasing order of He II optical thickness, specifically: component 3+4 lying closest, followed by 2, then 1. Similarly, the absence of the blueshifted components during high flux states of NGC 3516 is consistent with them being screened by gas that is optically thick during low flux states, and hence we chose to have them positioned outside the core components.

We have attempted to model each kinematic component as a single zone, adding additional zones only when necessary. As typical in such analyses, the resulting model parameters are a possible, but not necessarily unique, solution set. However, the dual constraints of screening and the total X-ray opacity significantly reduce the parameter space for the models. Finally, the true test for this geometry and physical parameters is whether such a model can replicate the high-state column densities, as we discuss in Section 4.3.

4. Model Results

4.1. The UV Absorbers

The model parameters for each component, including U , N_H , and $\langle T_e \rangle$ (the mean electron temperature), are listed in Table 5. Implicit in our assumptions is that the distances between these components are significantly smaller than their average radial distance, i.e., they are roughly co-located. Also, note that the predicted temperatures are sensitive to the choice of density and, hence, should be considered as very rough approximations.

The predicted ionic columns for each component are compared to the measured values in Table 6 (for the full set of predicted column densities for the core components, see Tables 7 through 10). For component 3+4, N_H and U were constrained by the lower limits to $N_{H\ I}$, $N_{C\ IV}$ and $N_{N\ V}$, and the upper limit to $N_{Si\ IV}$ (see Table 3). Component 2 is ionized by the continuum transmitted by 3+4, and is constrained by the value of $N_{Si\ IV}$, as well as the aforementioned lower limits. Both of these components were successfully modeled as single-zoned absorbers.

For component 1, a single-zoned model underpredicts C II, while overpredicting Mg II. This is a result of the ionization structure of the slab interior to the point where the gas becomes optically thick at the He II Lyman limit (54.4 eV). At this point most of the magnesium is in the form of Mg III, which has an ionization potential of 80 eV, little of which can be ionized to Mg IV by the heavily absorbed ionizing continuum. On the other hand, most of the carbon is C IV, since C III has an ionization potential of 47.7 eV, i.e., below that of He II. Hence, while Mg II is populated by recombination of Mg III, there is little C II, due to the relatively small fraction of carbon in the form of C III. If the ionization parameter is significantly lower, the higher ionization states are less populated due to the paucity of ionizing photons, and the situation is mitigated, in the sense that the C III and

Mg III zones overlap more completely. Hence, we used a two-zoned model to fit component 1. The choice of parameters for the two components is somewhat arbitrary, however, for the sake of simplicity, we assumed that the N V, C IV, and Si IV arise in one component (1A), while the C II and Mg II are formed in the other (1B). Note that, while the prediction for $N_{C\ II}$ is quite good, the model overpredicts $N_{Mg\ II}$ by a factor of ~ 3.5 . This may be the consequence of our assumption of solar abundances, as we discuss in Section 5.2.

Interestingly, components 1A and 1B predict a combined neutral column of $N_{H\ I} \approx 10^{17}\text{ cm}^{-2}$, which is less than half the column determined from the 1995 HUT spectrum (Kriss et al. 1996a). Part of the difference may be due to the contribution from component 2, since these components are not separable at low resolution. However, the continuum flux observed by HUT was roughly a factor of two higher than in the STIS spectra and, as we discuss in Section 4.2, the total neutral column should, therefore, have been lower. Nevertheless, we do not detect any additional low ionization lines in the STIS spectra that might be associated with an unmodeled neutral component. This apparent discrepancy may be due to the presence of a small additional column of neutral gas within our line-of-sight during the time of the HUT observations.

As shown in Table 3, the $N_{N\ V}/N_{H\ I}$ and $N_{C\ IV}/N_{H\ I}$ ratios for the blueshifted components are unusual in the sense that both are large. Although H I columns can be quite small in very highly ionized gas ($U > 0.5$), the fractional populations of the lithium-like ionic states tend to be similarly small. In part, the unusual ionization balance in these components may be the result of illumination by a heavily absorbed continuum, which has very few photons with energies between 54.4 eV and 100 eV (see Figure 5). In this case, N V is produced by X-ray ionization of N IV by photons with energies much greater than its ionization potential; the photoionization cross-section at these energies is much lower than at the threshold energy. To overcome this inefficiency, the ionization parameter must

be high (> 0.5), which in turn ionizes a greater fraction of the hydrogen than in gas exposed to an unfiltered continuum.

While the N_{NV}/N_{CIV} ratios for the blueshifted components are well-fitted by the models, N_{HI} is underpredicted for component 5, and overpredicted for the other components. It must be noted that the overpredictions are *much* worse when an unfiltered continuum is used (we did not include the effects of continuum filtering between these components, but they are all optically thin at the He II Lyman limit, so the effect is negligible). Somewhat more curious, given the casual similarity of these absorption features, is the large range in N_H and U (see Table 5). However, these components experienced an extreme drop in the ionizing flux, due to the drop in the intrinsic continuum luminosity and the increase in opacity of the intervening gas, over which time they may have undergone large temperature changes (see Section 5.2). It is possible that the apparently peculiar ionization balance in these components is a result of this recent history. Therefore, we only list the predicted columns for component 5, which is the lowest ionization and most thermally stable (which may explain why the predicted column densities are the most accurate).

4.2. Origin of the X-ray Absorption

Our models for the core components predict significant column densities for C VI, N VI, O VI, and O VII, hence, significant X-ray opacities. As shown in Figure 5, the large He II column suppresses the soft-X-ray flux. Finally, the total column density for these components is $N_H = 7.7 \times 10^{21} \text{ cm}^{-2}$, which is nearly identical to the single zone model described in Paper I. So, it is likely that the UV absorbers are responsible for the X-ray absorption.

A full and detailed analysis of the X-ray spectra from NGC 3516 has already been presented in Paper I. We do not consider it necessary to repeat such an analysis here. However, in order to test and illustrate the hypothesis that the UV absorbers and X-ray absorbers are dominated by the same components, we have performed direct comparisons of the models and data. The ionic column densities for each of the core components (see Tables 7 – 10) were used to predict the bound-free absorption edges in the X-ray band using the analytic expressions of Verner & Yakovlev (1995) and Verner et al. (1997). We have excluded the blueshifted components since we have not constrained their physical states, although it is our belief that their column densities are too low to contribute much to the X-ray absorption. These were compared to the X-ray data assuming a Galactic column density of $2.9 \times 10^{20} \text{ cm}^{-2}$ appropriate for this line of sight (Murphy et al 1996).

It should be stressed that this direct and simple comparison does *not* include the additional spectral components discussed in the more detailed treatment of Paper I. Specifically, here we do not include the Compton “reflection” from optically-thick material which is likely to dominate the observed X-ray spectrum $\gtrsim 5 \text{ keV}$, or any emission from any other circumnuclear material.

Nevertheless assuming the SED described in Section 3.1, we find our column densities for the low-state spectrum produce a predicted X-ray spectrum similar to that of Paper I. Thus our model provides a comparable (acceptable) description of the *CXO/LEGTS* data to that shown in Paper I, and is strong evidence that the UV and X-ray absorption arise in the same gas, as suggested by Mathur et al. (1997), although the absorber consists of multiple zones, characterized by different ionization parameters and column densities, as discussed in Kriss et al. (1996a). Also interesting is the lack of evidence for highly ionized gas (e.g., $U \sim 1$, $N_H > 10^{21} \text{ cm}^{-2}$) within the line-of-sight to the active nucleus in NGC 3516, in contrast to NGC 3783 (Kaspi et al. 2000), NGC 5548 (Kaastra et al. 2000), and

NGC 4051 (Collinge et al. 2001).

4.3. Variability of the Absorbers

In Paper I, we argued that the differences in the X-ray properties of NGC 3516 in the *CXO*/LETGS spectrum compared to earlier *ASCA* spectra were due to variations in the continuum flux and the corresponding changes in the ionization state and, therefore, opacity of the intervening absorber. Since we have established that the UV and X-ray absorption occur in the same gas, it follows that the changes in UV absorbers must also be in response to variations in ionizing flux, rather than variations in total column density. As noted above, the continuum flux at 1460 \AA was roughly 4.5 times greater in the GHRS observations than during the STIS GTO observations, and represents the AGN in a high state. We assumed that the flux at the Lyman limit scaled by the same factor. As there were no contemporaneous X-ray observations, we assumed that the 0.5 keV flux increased by a factor of 9, as suggested in Paper I. Finally, we assumed that the α remained $= -1.0$ between 13.6 eV and 100 eV, which requires a change in α to -1.87 from 100 eV to 500 eV (although, clearly, we do not know how the SED may have changed in the EUV to soft X-ray band). Through an iterative analysis of the 1994 *ASCA* spectrum, we set the 0.5 to 10 keV spectral index to -0.89 .

In modeling the absorbers we held the column densities fixed and assumed the same relative positions. The high-state continuum increased Q , and thus U for the unscreened gas, by a factor of ≈ 4.6 . The predicted values of $N_{C IV}$ for the core components are given in Table 6, and match the GHRS values well, although the prediction for component 2, while still indicative of saturation, is slightly below the lower limit (which may be indicative of a somewhat larger column density in the earlier epoch, as suggested by the limits on $N_{H I}$ determined from the HUT spectrum [Kriss et al. 1996a]). Interestingly, in the low-state

models, all the C IV associated with component 1 was from the higher ionization zone, while in the high-state both zones of component 1 contribute to it. The high-state model for component 5 predicts a negligibly small value for $N_{C\ IV}$, so the absence of the blueshifted components can also be explained by the higher ionizing flux.

As with the low-state models, we have taken the predicted column densities (see Tables 11 – 14) and used them to model the *ASCA* data obtained in 1994 April (e.g. George et al. 1998) when the nucleus of NGC 3516 was a factor of 8 to 10 (at ~ 6 keV) brighter (and the Compton ”reflected” continuum less important). We followed the standard procedures for the reduction and analysis of *ASCA* data, ignoring the 5–7 keV band (where there is emission from Fe $K\alpha$), and fitting the time-averaged spectral data from all four *ASCA* detectors simultaneously. Only the spectral index and normalization of the underlying power law continuum was allowed to vary during the analysis (the bound-free absorption appropriate for the ”high-state” column densities were fixed at the values predicted by the UV models). As expected, the index of the continuum was in good agreement with our assumptions concerning the SED ($1.87 \lesssim \Gamma \lesssim 1.89$ at 90% confidence). The resulting fit is shown in Figure 6, and it again matches the overall spectral characteristics. Given the source is variable in both the X-ray band, and in the overall shape of the SED, and that there are no simultaneous high resolution UV measurements, we consider our predictions to be in remarkable agreement with the X-ray observations at this epoch.

5. Discussion

5.1. Geometry of the Circumnuclear Gas

We have shown that our model for the UV absorbers, with the components arranged in increasing radial distance and each covering the continuum source, accurately predicts

most of the ionic columns and the X-ray opacity. Given the success of the model, we may use it as a starting point to unravel the geometry of the circumnuclear gas. In paper I, based on the recombination timescale for O VII, we placed a conservative lower limit on the density of X-ray absorber of $n_H \geq 2 \times 10^6 \text{ cm}^{-3}$. For component 1B, we predict that $N_{C \text{ III}} = 1.87 \times 10^{15} \text{ cm}^{-2}$. The lack of detection of C III* 1175 is indicative of $N_{C \text{ III}^*} \lesssim$ a few $\times 10^{13} \text{ cm}^{-2}$. For $T \sim 2.0 \times 10^4 \text{ K}$, this ratio of $N_{C \text{ III}^*}/N_{C \text{ III}}$ corresponds to a density of $\lesssim 10^{10} \text{ cm}^{-2}$ (Bromage et al. 1985; Kriss et al. 1992). If the high-ionization core components are co-located with component 1b, their higher ionization parameters require that they have densities of $\lesssim 10^8 \text{ cm}^{-3}$. Alternatively, for component 1A, we predict that $N_{C \text{ III}} = 9.43 \times 10^{15} \text{ cm}^{-2}$. Based on the upper limit for $N_{C \text{ III}^*}$, the density of component 1A is $< 10^{9.5} \text{ cm}^{-3}$. Hence, we derive a loose upper limit of $n_H \lesssim 10^9 \text{ cm}^{-3}$ for the density of the high-ionization core components. Given our estimate of the continuum luminosity and the constraints on the densities of the absorbers, the core components must lie between $5.4 \times 10^{16} \text{ cm}$ and $1.2 \times 10^{18} \text{ cm}$ from the central source. This range in radial distance is consistent with full-covering of the broad C IV emission region, which has a radius of ~ 4.5 light-days (Koratkar et al. 1996). By comparison, Kraemer et al. (2001a) estimated that the high density ($n_H \geq 10^{9.5} \text{ cm}^{-3}$) UV absorber detected in NGC 4151, component D+E, must lie at a distance of $\lesssim 6.2 \times 10^{16} \text{ cm}$ from the central source (assuming $H_0 = 75 \text{ km s}^{-1} \text{ Mpc}^{-1}$). Hence, the radial distance of the absorbing gas in NGC 3516 is roughly consistent with that in NGC 4151, although possibly somewhat further from the central source and, apparently, less dense. On average, the absorbers are in a much higher ionization state than component D+E, for which $U = 0.015$. Since the ionizing luminosity of NGC 3516 is only a factor of ~ 2 greater than NGC 4151, observed in similar low-flux states, the greater ionization state must be mostly due to the lower density. Another interesting difference is the weakness of the scattered light in the troughs of the saturated absorption lines in NGC 3516: $< 5\%$ of the low-state continuum flux, compared to $\geq 50\%$ of the low-state

flux in NGC 4151 (Kraemer et al. 2001a). For NGC 4151, we argued that the scattered light consisted of continuum + broad-line emission, reflected into our line-of-sight by free electrons in a component of highly ionized gas that extended beyond the region covered by the absorbers. Either this component is weaker in NGC 3516, the absorbers are covering more of the scattering region, or the scattering region is further away from the nucleus (outside our projected aperture).

The observed emission-line fluxes can be used to constrain the global covering factor of the absorbers. The observed C IV λ 1550 flux is $\approx 2.37 \times 10^{-12}$ ergs cm $^{-2}$ s $^{-1}$, or $L_{C\ IV} \approx 3.5 \times 10^{41}$ ergs s $^{-1}$. For a density of $n_H = 10^8$ cm $^{-3}$, the radial distance of component 3+4 is $R = 1.7 \times 10^{17}$ cm and the predicted C IV flux at the illuminated surface of the 4 core component models absorbers is 1.5×10^6 ergs cm $^{-2}$ s $^{-1}$, hence, the covering factor must be ≤ 0.64 . Interestingly, in its current low-flux state, approximately 50% of the C IV emission is from a component with FWHM of ~ 1500 km s $^{-1}$ (see Figure 2 and Hutchings et al. [2001]), which is characteristic of the so-called intermediate line region (ILR; Wills et al. [1993]). If the absorbers are the source of the ILR emission, the covering factor is ~ 0.3 . Note, that although the core components cover both the broad and intermediate line contributions to the C IV emission, this does not imply that they must lie outside the ILR. For example, self-absorption by the ILR gas could occur in an expanding shell (see Hutchings et al. 2001). If the absorption arises in the ILR, the ILR gas has a significant radial velocity component, similar to the emission-line gas in the inner NLR of other Seyfert galaxies (Crenshaw & Kraemer 2000; Kaiser et al. 2000; Crenshaw et al. 2000b; Ruiz et al. 2001). A connection between the ILR and NLR components has been suggested by Sulentic & Marziani (1999), although our results suggest that the ILR could extend to the outer edge of the BLR.

5.2. The Source of the Reddening

From our estimate of the intrinsic reddening (see Section 4.1), one would infer that there is a component of dusty gas of column density $N_H \sim 3 \times 10^{20} \text{ cm}^{-2}$ along our line-of-sight to the nucleus of NGC 3516. Note that this is based on assumption of a Galactic dust/gas ratio; if the ratio were lower, the column would be larger. As shown in Kraemer et al. (2000) and Crenshaw et al. (2001), UV absorption lines can form in dusty gas surrounding an AGN. Typically, one would expect strong C IV lines from a column of this size. Hence, either the absorption lines associated with the dusty column are buried in the troughs of the core components, or the dust exists in one or more of these absorbers.

Following Barvainis (1987), we can estimate the dust sublimation radius, i.e, the point interior to which dust grains would evaporate. During its low-flux state, the ionizing luminosity of the central source is $\sim 1.4 \times 10^{43} \text{ ergs s}^{-1}$. Assuming an average luminosity a factor of 3 greater (see Section 2.3), and a dust sublimation temperature of 1500 K (Salpeter 1977), the sublimation radius for NGC 3516 is $\lesssim 2.6 \times 10^{17} \text{ cm}$, or, roughly the same radial distance as the core components. Although the absorbers are radially outflowing, we do not know their starting point, or whether they were well-shielded from the continuum source by intervening gas. Hence it is possible that some grains have survived within them. Alternatively, some dust could have been swept-up by the absorbers as they move outwards. If, for example, the dust were within component 1, it may help explain the overprediction of Mg II (section 4.1). Furthermore, since the column density of component 1 is roughly 5 times larger than our dusty column, the dust/gas ratio could be 20% the Galactic ratio (indicative of the harsh conditions close to the active nucleus), and still produce the observed reddening. In any case, although it is possible the dust is in a heretofore undetected component of gas, we suggest that the reddening may be due to a small amount of dust within one or more of the core components.

5.3. The Nature of the Outflow

Perhaps the most unusual aspect of the intrinsic absorption in Seyfert galaxies is the lack of evidence for radial acceleration. In the case of NGC 4151, Weymann et al. (1997) attributed this to the large radial distances of the absorbers. However, in Kraemer et al. (2001a) we determined that component D+E was close enough to the central source that it should undergo a detectable acceleration. To explain this, we suggested that the large column density and optical thickness of D+E would make radiative acceleration inefficient (see Williams 1972; Mathews 1974). The physical conditions in the core components of NGC 3516 are similar to D+E, hence the absence of detectable changes in radial velocities between 1995 and the present is understandable, although it is interesting that the blueshifted components, which only appear during lowstates, appear at generally the same velocities, and these are clearly optically thin (of course, the radial acceleration of the absorbers may simply be too small to detect in the ~ 6 years between the GHRS and STIS observations). Another explanation is that the absorbers are not simply radially (or even radiatively) accelerated. Disk-wind models (e.g., Konigl & Kartje 1994) require that the gas in the outflow must first be levitated off the accretion disk. Bottorff, Korista, & Shlosman (2000) have modeled the absorbers as part of a magnetohydrodynamic wind, which has a strong non-radial component. Elvis (2000) has also proposed an outflow scenario that includes a non-radial component.

If the absorption arises in disk-driven wind, the gas would have a strong transverse component of velocity. However our analysis (see also Paper I) suggests strongly that the variability of the absorption in NGC 3516 results from changes in ionization state due to the variable luminosity of the central source, rather than changes in column density due to transverse motion. One possibility is that the individual kinematic components are associated with different flow tubes or shells along our line-of-sight, which would originate

at different radial positions at the base of the wind. Since the total column density within the absorber does not appear to change, the amount of gas within these tubes must be fairly constant, although this does not imply confinement but, rather, a continuous flow. Although the source luminosity changes dramatically, the flow density appears to be independent of the short-term changes in the flux, which may imply that it is not radiatively driven off the disk (see, again, Bottorff et al. 2000).

Interestingly, in our model the radial velocities of components 1 through 5 increase with distance from the central source. This would be expected if they each originated at the roughly the same distance, and have been continuously accelerated, e.g., via resonance line driving or some other radiative mechanism. However, the velocities can also depend on the radial distance at which the different components originated, hence a range in velocities may not be an indication of acceleration, but of different “launch-pads” for the components of the flow.

Another interesting aspect of the UV absorbers is their apparent stability; the core components vary in ionization state but have shown evidence for significant C IV columns for two decades. As discussed in Krolik, Mckee, & Tarter (1981) and, more recently, in Krolik & Kriss (2001), there are two regimes of ionization (characterized by the “pressure” ionization parameter, or U/T) and temperature wherein a cloud of photoionized gas is stable to thermal perturbations: at low ionization/temperature, when line cooling is efficient, and at high temperature/ionization, when thermal balance is achieved via Compton processes. In the intermediate region, small changes in ionization can result in large changes in temperature. Although the exact relationship between U/T and T for a model nebula depends on the SED of the continuum radiation, including the non-ionizing continuum which is critical in the Compton regime, and the atomic parameters, such as collision strengths, instability typically occurs between 5×10^4 K and 10^7 K. Both our

low- and high-state models for the core components predict that these absorbers remain thermally stable, which may help explain their continuing presence. On the other hand, the blueshifted components may not be stable. In Figure 7, we show the instability curve for the screened SED used for the models of the blueshifted components. In the current low-state, component 5 is in the low-temperature stable regime, while the more highly ionized components lie along the vertical, quasi-stable, region (unstable regions are places where $dT/dU < 0$). This implies that these components have experienced large temperature fluctuations in response to the changes in ionizing flux, which may explain part of the discrepant model predictions. Perhaps most of this gas is in the Compton-cooled state, out of which UV absorbers condense when the continuum flux drops sufficiently. The variable opacity of the intervening core components amplifies the changes in ionizing flux and, hence, thermal perturbations of the blueshifted components.

6. Summary

We have used medium-resolution echelle spectra obtained with *HST*/STIS to study the physical conditions in the UV absorbers in the Seyfert 1 galaxy, NGC 3516 while it was in a recent low-continuum state. We have used contemporaneous *CXO*/LETG data (discussed in Paper I) to examine the connection between the UV and X-ray absorbers, and have compared our model results to archival, high-state GHRs and *ASCA* spectra.

We find that the bulk of the UV and X-ray absorption arises in the same gas, principally components 1,2, and 3+4. The line-of-sight covering factors for these components are all > 0.9 , hence they must be screening one another from the ionizing source. We have demonstrated that the historical changes in the properties of the absorbers are due to changes in their ionization state in response to different levels of the ionizing flux. The changes are more dramatic for the screened components, which are also affected by the

changes in opacity of the intervening gas. In particular, the disappearance of components 5 – 8 in C IV (the variable blueshifted absorption seen in *IUE* spectra) is due to the much higher ionization parameters at high states, as a result of the much lower opacities of components 1 –4.

Although there are apparent similarities between NGC 3516 and NGC 4151, such as linear radio structure (Nagar & Wilson 1998), NLR kinematics (Ruiz et al. in preparation), and central source luminosity, there are striking differences in the appearance of their UV spectra. First, unlike NGC 4151 (see Kraemer et al. 2001a), there is little evidence for scattered continuum radiation in a $0''.2 \times 0''.2$ aperture centered on the nucleus; alternatively, the absorbers are *covering* the scattering region. Second, in Kraemer et al. (2001a) we argued that the X-ray absorption in NGC 4151 was due to a component of highly ionized gas which we were unable to identify among the UV absorbers, which is clearly not the case for NGC 3516. Finally, the absorbers in NGC 3516 are both in a higher ionization state and of lower density than those in NGC 4151. It will be interesting if these differences are intrinsic to these otherwise similar AGN, or are a clue to the nature of mass outflow.

S.B.K. and D.M.C. acknowledge support from NASA grant NAG5-4103. H.N. acknowledges support by ISF and by UMBC. T.J.T. acknowledges support for NASA grant NAG5-7538. S.B.K. thanks Gary Ferland and Fred Bruhweiler for illuminating discussions. We thank Jay Dunn for help with the tables. We thank an anonymous referee for their careful reading of the manuscript and useful comments.

REFERENCES

- Barvainis, R. 1987, *ApJ*, 320, 537
- Bottorff, M.C., Korista, K., & Shlosman, I. 2000, *ApJ*, 537, 134
- Brandt, W.N., Fabian, A.C., & Pounds, K.A. 1996, *MNRAS*, 278, 326
- Bromage, G.E., et al. 1985, *MNRAS*, 215, 1
- Brotherton, M.S., et al. 2002, *ApJ*, 565, 800
- Clavel, J., et al. 1991, *ApJ*, 366, 64
- Collinge, M.J., et al. 2001, *ApJ*, 557, 2
- Crenshaw, D.M., et al. 1996, *ApJ*, 470, 322
- Crenshaw, D.M., et al. 2000a, *ApJ*, 545, L27
- Crenshaw, D.M., et al. 2000b, *AJ*, 120, 1731
- Crenshaw, D.M., et al. 2002, *ApJ*, 566, 187
- Crenshaw, D.M., Maran, S.P., & Mushotzky, R.F. 1998, *ApJ*, 496, 797
- Crenshaw, D.M., & Kraemer, S.B. 1999, *ApJ*, 521, 572
- Crenshaw, D.M., & Kraemer, S.B. 2000, *ApJ*, 532, L101
- Crenshaw, D.M., Kraemer, S.B., Boggess, A., Maran, S.P., Mushotzky, R.F., & Wu, C.-C. 1999, *ApJ*, 516, 750
- Crenshaw, D.M., Kraemer, S.B., Bruhweiler, F.C., & Ruiz, JR. 2001, *ApJ*, 555, 633
- Edelson, R., et al. 2000, *ApJ*, 534, 180
- Elvis, M. 2000, *ApJ*, 545, 63
- Espey, B.R., Kriss, G.A., Krolik, J.H., Zheng, W., Tsvetanov, Z., & Davidsen, A. 1998, *ApJ*, 500, L13

- Ferland, G.J., et al. 1998, *PASP*, 110, 761
- George, I.M., Turner, T.J., Netzer, H., Nandra, K., Mushotzky, R.F., & Yaqoob, T. 1998, *ApJS*, 114, 73
- Goad, M.R., et al. 1999, *ApJ*, 524, 707
- Grevesse, N., & Anders, E. 1989, in *Cosmic Abundances of Matter*, ed. C.J. Waddington (New York: AIP), 1
- Hamann, F., Barlow, T.A., Junkkarinen, V., & Burbidge, E. M. 1997, *ApJ*, 478, 78
- Hutchings, J.B., et al. 2001, *ApJ*, 559, 173
- Kaastra, J.S., Mewe, R., Liedahl, D.A., Komossa, S., & Brinkman, A.C. 2000, *A&A*, 354, L83
- Kaiser, M.E., et al. 2000, *ApJ*, 528, 260
- Kaspi, S., Brandt, W.N., Netzer, H., Sambruna, R., Chartas, G., Garmire, G.P., & Nousek, J.A. 2000, *ApJ*, 535, L17
- Kolman, M., Halpern, J.P, & Martin, C. 1993, *ApJ*, 403, 592
- Konigl, A., & Kartje, J.F. 1994, *ApJ*, 434, 446
- Koratkar, A., et al. 1996, *ApJ*, 470, 378
- Kraemer, S.B., Crenshaw, D.M., & Gabel, J.R. 2001b, *ApJ*, 557, 30
- Kraemer, S.B., et al. 2001a, *ApJ*, 551, 671.
- Kraemer, S.B., George, I.M., Turner, T.J., & Crenshaw, D.M. 2000, *ApJ*, 535, 53
- Kriss, G.A., Espey, B.R., Krolik, J.H., Tsvetanov, Z., Zheng, W., & Davidsen, A.F. 1996b, *ApJ*, 467, 622
- Kriss, G.A., et al. 1992, *ApJ*, 392, 485
- Kriss, G.A., et al. 1996a, *ApJ*, 467, 629

- Kriss, G.A., et al. 2000, ApJ, 538, L17
- Krolik, J.H., & Kriss, G.A. 1995, ApJ, 447, 512
- Krolik, J.H., & Kriss, G.A. 2001, ApJ, 561, 684
- Krolik, J.H., Mckee, C.F., & Tarter, B. 1981, ApJ, 249, 422
- Lindler, D. 1998, CALSTIS Reference Guide (CALSTIS Version 5.1)
- Mathews, W.G. 1974, ApJ, 189, 23
- Mathis, J.S., Rumpl, W., & Nordsieck, K.H. 1977, ApJ, 217, 425
- Mathur, S., Wilkes, B.J., & Aldcroft, T. 1997, ApJ, 478, 182
- Murphy, E.M., Lockman, F.J., Laor, A., Elvis, M. 1996, ApJS, 105, 369
- Nagar, N., & Wilson, A.S. 1998, ApJ, 516, 97
- Nandra, K., & Pounds, K.A., 1994, MNRAS, 268, 405
- Netzer, H., Chelouche, D., George, I.M., Turner, T.J., Crenshaw, D.M, Kraemer, S.B., & Nandra, K. 2002, ApJ, in press (Paper I)
- Otani, C., et al. 1996, PASP, 48, 211
- Pitman, K.M., Clayton, G.C., & Gordon, K.D. 2000, PASP, 112, 537
- Reynolds, C.S. 1997, MNRAS, 286, 513
- Reynolds, C.S., Ward, M.J, Fabian, A.C., & Celotti, A. 1997, MNRAS, 286, 513
- Ruiz, J.R., Crenshaw, D.M., Kraemer, S.B., Bower, G.A., Gull, T.R., Hutchings, J.B., Kaiser, M.E., & Weistrop, D. 2001, AJ, 122, 2961
- Salpeter, E.E. 1977, ARA&A, 15, 267
- Savage, B.D., & Mathis, J.S. 1979, ARA&A, 17, 73
- Schlegel, D.J., Finkbeiner, D.P, & Davis, M. 1998, ApJ, 500,525

- Shull, J.M., & van Steenberg, M. 1982, ApJS, 48, 95
- Sulentic, J.W., & Marziani, P. 1999, ApJ, 518, L9
- Ulrich, M.-H., & Boisson, C. 1983, ApJ, 267, 515
- Verner, D.A., Yakovlev, D.G., 1995, A&AS, 109, 125
- Verner, D.A., Ferland, G.J., Korista, K.T., Yakovlev, D.G., 1997, ApJ, 465, 487
- Voit, G.M., Shull, J.M., & Begelman, M.C. 1987, ApJ, 316, 573
- Walter, R., Ulrich, M.-H., Courvoisier, T.J.-L., & Buson, L.M. 1990, A&A, 233, 53
- Weymann, R.J., Morris, S.L., Gray, M.E., & Hutchings, J.B. 1997, ApJ, 483, 717
- Williams, R.E. 1972, ApJ, 178, 105
- Wills, B.J., Brotherton, M.S., Fang, D., Steidel, C.C., & Sargent, W.L.W. 1993, ApJ, 415, 563
- Wills, B.J., et al. 1985, ApJ, 288, 94

Fig. 1.— GHRs (blue and red lines) and STIS (black line) spectra of the C IV region in NGC 3516. The kinematic components of the intrinsic C IV absorption doublet that were originally detected in the GHRs spectra are numbered.

Fig. 2.— Portions of the STIS echelle spectra of NGC 3516, showing the intrinsic absorption lines in different ions. Fluxes are plotted as a function of the radial velocity (of the strongest member, for the doublets), relative to an emission-line redshift of $z = 0.00875$. The kinematic components are identified for the strong members of the doublets, and vertical dotted lines are plotted at their approximate positions. Strong Galactic absorption lines are labeled. The unocculted NLR profiles discussed in Section 2.2 are overplotted in red.

Fig. 3.— Far-UV continuum light curve of NGC 3516. Fluxes ($\text{ergs s}^{-1} \text{cm}^{-2} \text{\AA}^{-1}$) at 1460\AA are plotted as a function of Julian date. The pluses are from *IUE*, and the X's are from the other satellites; vertical lines indicate the error bars (\pm one sigma).

Fig. 4.— Averaged *IUE* spectra in the C IV region at three different continuum flux states (black lines). For comparison, rebinned spectra from the GHRs high state and STIS low state (red lines) are overplotted.

Fig. 5.— Low (lower part of panel) and High (upper part of panel) state model ionizing continua. The solid line represents the continuum incident upon component 3+4, while the dotted line is the continuum transmitted by component 1.

Fig. 6.— Fits to the 1994 *ASCA* (high level) and 2000 *CXO/LETGS* (low level) observations, based on the predictions of the UV absorbers models. No attempt has been made to fit the the Fe $K\alpha$ emission near 6.4 keV.

Fig. 7.— Thermal stability curve for models generated with the same SED used for the low-state (solid line) and high-state (dash-dotted line) component 5 models. The flat

sections, at low and high temperature, are the stable line-cooled and Compton-cooled regions, respectively. The symbols are the location of our best-fit models for component 5 at the low and high flux states. Note that the very steep rise for T is $> 10^5$ K in the low-state curve is due to the effects of the screened SED.

Table 1. *HST* High-Resolution Spectra of NGC 3516

| Instrument | Grating | Coverage (Å) | Resolution ($\lambda/\Delta\lambda$) | Exposure (sec) | Date (UT) | (MJD) |
|------------|---------|--------------------------|---|-------------------|-----------------|-----------|
| STIS | E140M | 1150 – 1730 | 46,000 | 5488 | 2000 October 1 | 2451819.5 |
| STIS | E230M | 2275 – 3120 | 30,000 | 2220 | 2000 October 1 | 2451819.5 |
| GHRM | G160M | 1529 – 1597 ^a | 20,000 | 7296 ^b | 1995 April 25 | 2449833.5 |
| GHRM | G160M | 1529 – 1597 ^a | 20,000 | 6084 ^b | 1995 October 22 | 2449833.5 |

^aCovers the C IV region (Crenshaw et al. 1998, 1999).

^bper grating setting; two settings were used.

Table 2. Absorption Components in NGC 3516

| Component | Velocity ^a (km s ⁻¹) | FWHM (km s ⁻¹) | C _{los} ^b |
|-----------|--|-------------------------------|-------------------------------|
| 1 | -376 (±7) | 70 (±8) | 0.98 (±0.02) |
| 2 | -183 (±8) | 44 (±10) | 0.98 (±0.02) |
| 3+4 | -36 (±4) | 20 (±4), 31 (±5) ^c | 0.95 (±0.02) |
| 5 | -1372 (±9) | 271 (±44) | 0.81 (±0.21) |
| 6 | -994 (±16) | 36 (±6) | ————— |
| 7 | -837 (±7) | 99 (±16) | ————— |
| 8 | -692 (±4) | 35 (±5) | ————— |

^aVelocity centroid for a systemic redshift of $z = 0.00875$.

^bCovering factor in the line of sight from the core of the C IV doublet.

^cFrom GHRs components 3 and 4, respectively (see Crenshaw et al. 1999).

Table 3. Measured Ionic Column Densities (10^{14} cm^{-2})

| Comp. | Ly α | N V | C IV | Si IV | C II | C II* | Mg II |
|-------|-----------------|-----------------|-----------------|-----------------|-----------------|-----------------|-----------------|
| STIS | | | | | | | |
| 1 | >5.99 | >20.48 | >10.26 | >1.86 | 0.79 ± 0.25 | 1.44 ± 0.30 | 0.05 ± 0.02 |
| 2 | >6.56 | >21.55 | >13.75 | 0.15 ± 0.05 | <0.25 | <0.25 | <0.02 |
| 3+4 | >3.34 | >4.84 | >6.20 | <0.04 | <0.25 | <0.25 | <0.02 |
| 5 | 0.97 ± 0.18 | 1.65 ± 0.39 | 2.11 ± 0.30 | <0.04 | <0.25 | <0.25 | <0.02 |
| 6 | 0.09 ± 0.04 | 0.29 ± 0.10 | 0.10 ± 0.04 | <0.04 | <0.25 | <0.25 | <0.02 |
| 7 | 0.31 ± 0.05 | 1.35 ± 0.24 | 0.31 ± 0.07 | <0.04 | <0.25 | <0.25 | <0.02 |
| 8 | 0.26 ± 0.04 | 0.48 ± 0.14 | <0.07 | <0.04 | <0.25 | <0.25 | <0.02 |
| GHRS | | | | | | | |
| 1 | | | >8.0 | | | | |
| 2 | | | >13.7 | | | | |
| 3 | | | 0.4 ± 0.1 | | | | |
| 4 | | | 0.5 ± 0.1 | | | | |

Table 4. Low-Resolution FUV Spectra of NGC 3516

| Instrument/ Grating | Coverage (Å) | Resolution ($\lambda/\Delta\lambda$) | Date (UT) | (MJD) |
|------------------------|-----------------|---|---|-----------------------|
| IUE SWP | 1150 – 1978 | ~250 | 1978 June 20 – 1995 April 14 ^a | 2443679.5 – 2449821.5 |
| HUT ^b | 820 – 1840 | ~450 | 1995 March 11 – 13 | 2449787.5 – 2449789.5 |
| FOS G130H | 1150 – 1605 | ~1200 | 1995 December 30 | 2450081.5 |
| FOS G130H | 1150 – 1605 | ~1200 | 1996 February 21 | 2450134.5 |
| FOS G130H | 1150 – 1605 | ~1200 | 1996 April 13 | 2450186.5 |
| FOS G130H | 1150 – 1605 | ~1200 | 1996 August 14 | 2450309.5 |
| FOS G130H | 1150 – 1605 | ~1200 | 1996 November 28 | 2450415.5 |
| STIS G140L | 1150 – 1715 | ~1000 | 1998 April 13 | 2450916.5 |
| STIS G140L | 1150 – 1715 | ~1000 | 2000 April 17 | 2451651.5 |

^aSee the IUE Merged Log at <http://archive.stsci.edu/iue>.

^bHopkins Ultraviolet Telescope (Kruk et al. 1995)

Table 5. Model Parameters

| Model | U | N_H (cm^{-2}) | $\langle T_e \rangle$ (K) |
|-------------------|-------|----------------------------|---------------------------|
| Low-state models | | | |
| 1A | 0.126 | 2.4e21 | 2.30e04 |
| 1B | 0.001 | 7.0e18 | 1.61e04 |
| 2 | 0.138 | 3.9e21 | 2.50e04 |
| 3+4 | 0.185 | 1.4e21 | 2.78e04 |
| 5 | 1.58 | 1.5e19 | 4.25e04 |
| 6 | 8.50 | 1.5e20 | 1.05e05 |
| 7 | 10.7 | 2.0e21 | 1.39e05 |
| 8 | 10.7 | 5.5e20 | 1.26e05 |
| High-state models | | | |
| 1A | 0.793 | 2.4e21 | 4.74e04 |
| 1B | 0.008 | 7.0e18 | 1.89e04 |
| 2 | 0.669 | 2.4e21 | 4.86e04 |
| 3+4 | 0.845 | 1.4e21 | 5.69e04 |
| 5 | 11.43 | 1.5e19 | 6.15e05 |

Table 6. Predicted Ionic Column Densities^a (10^{14} cm^{-2})

| Model | Ly α | N V | C IV | Si IV | C II | Mg II |
|--------------------------------|-------------------|-------------------|-------------------|-------------------|-------------------|-------------------|
| Low-state models (STIS epoch) | | | | | | |
| 1A | 7.52e02 | 6.85e01 | 2.03e03 | 1.96 | 0.09 | 0.05 |
| 1B | 3.06e02 | 0.03 | 2.72 | 0.46 | 2.23 | 0.14 |
| | (>5.99) | (>20.48) | (>10.26) | (>1.86) | (2.23 \pm 0.39) | (0.05 \pm 0.02) |
| 2 | 1.02e03 | 7.40e02 | 5.22e02 | 0.20 | 0.01 | – |
| | (>6.56) | (>21.55) | (>13.75) | (0.15 \pm 0.05) | (<0.25) | (<0.02) |
| 3+4 | 2.87e02 | 1.42e02 | 70.1 | – | – | – |
| | (>3.34) | (>4.84) | (>6.20) | (<0.04) | (<0.25) | (<0.02) |
| 5 | 0.30 | 1.59 | 2.13 | – | – | – |
| | (0.97 \pm 0.18) | (1.65 \pm 0.39) | (2.11 \pm 0.30) | (<0.04) | (<0.25) | (<0.02) |
| High-state models (GHRS epoch) | | | | | | |
| 1A | | | 4.58 | | | |
| 1B | | | 9.37 | | | |
| | | | (>8.0) | | | |
| 2 | | | 8.7 | | | |
| | | | (>13.7) | | | |
| 3+4 | | | 1.0 | | | |
| | | | (0.9 \pm 0.14) | | | |

^aThe values in parentheses are the measured column densities (see Table 3).

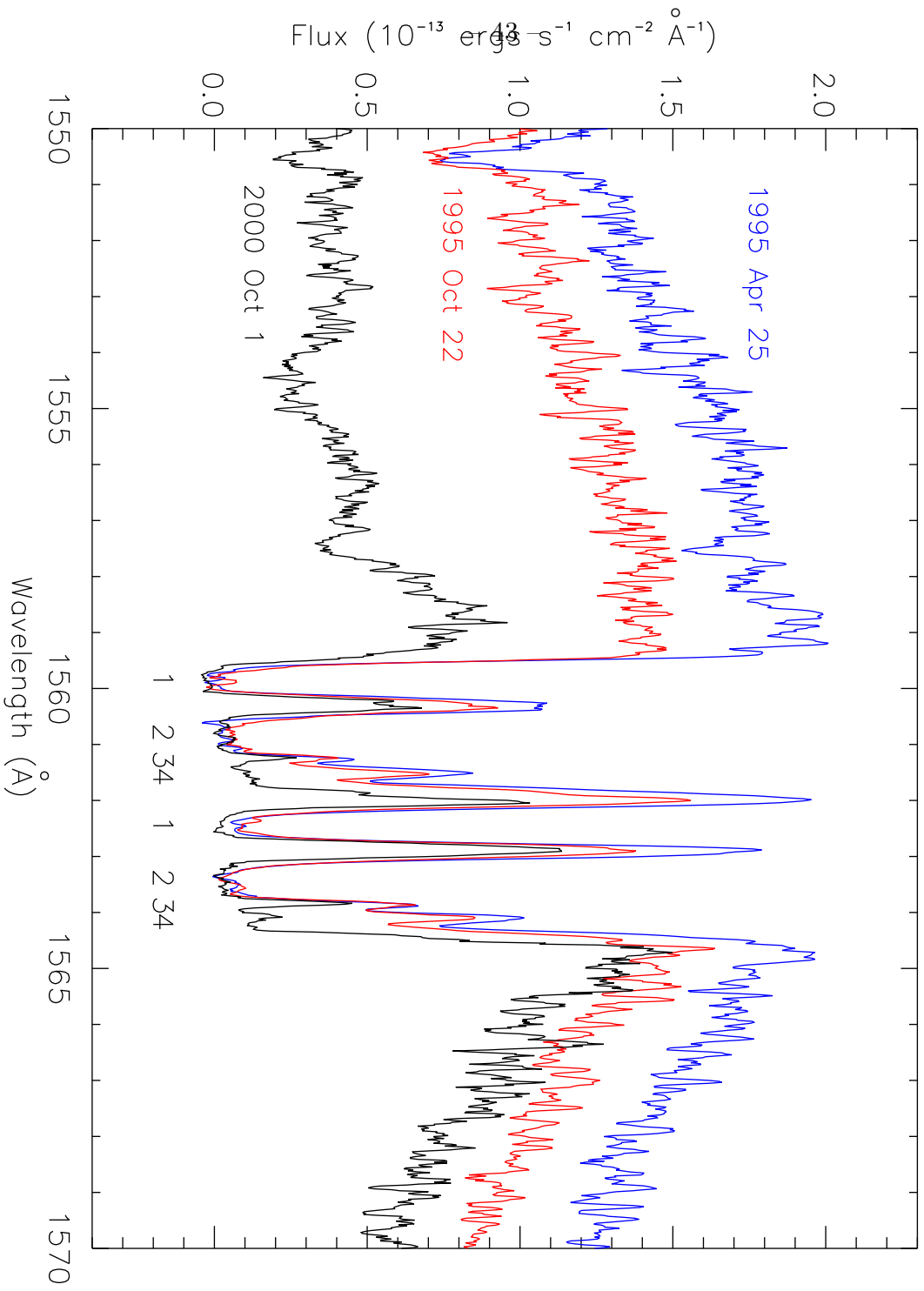


Fig. 1.

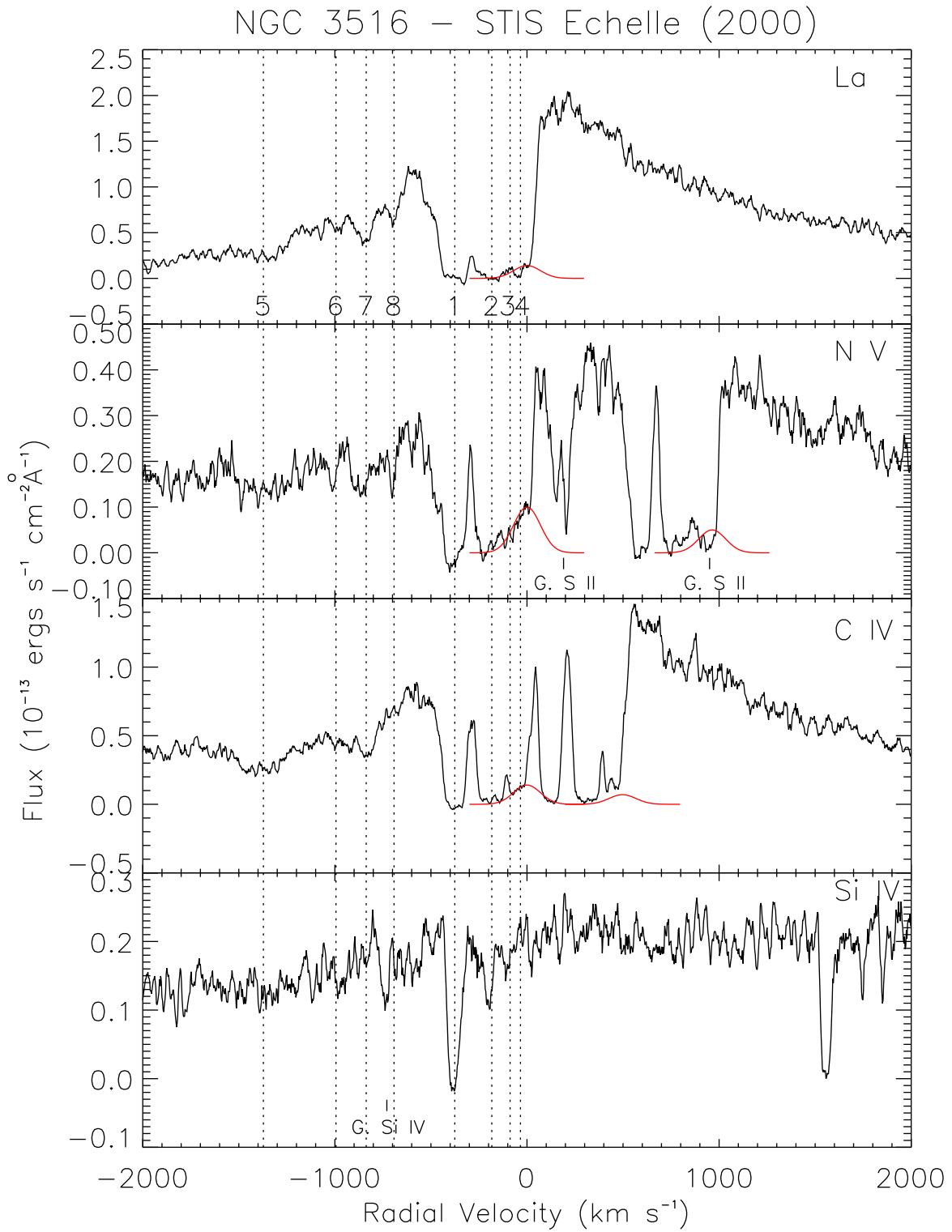


Fig. 2.

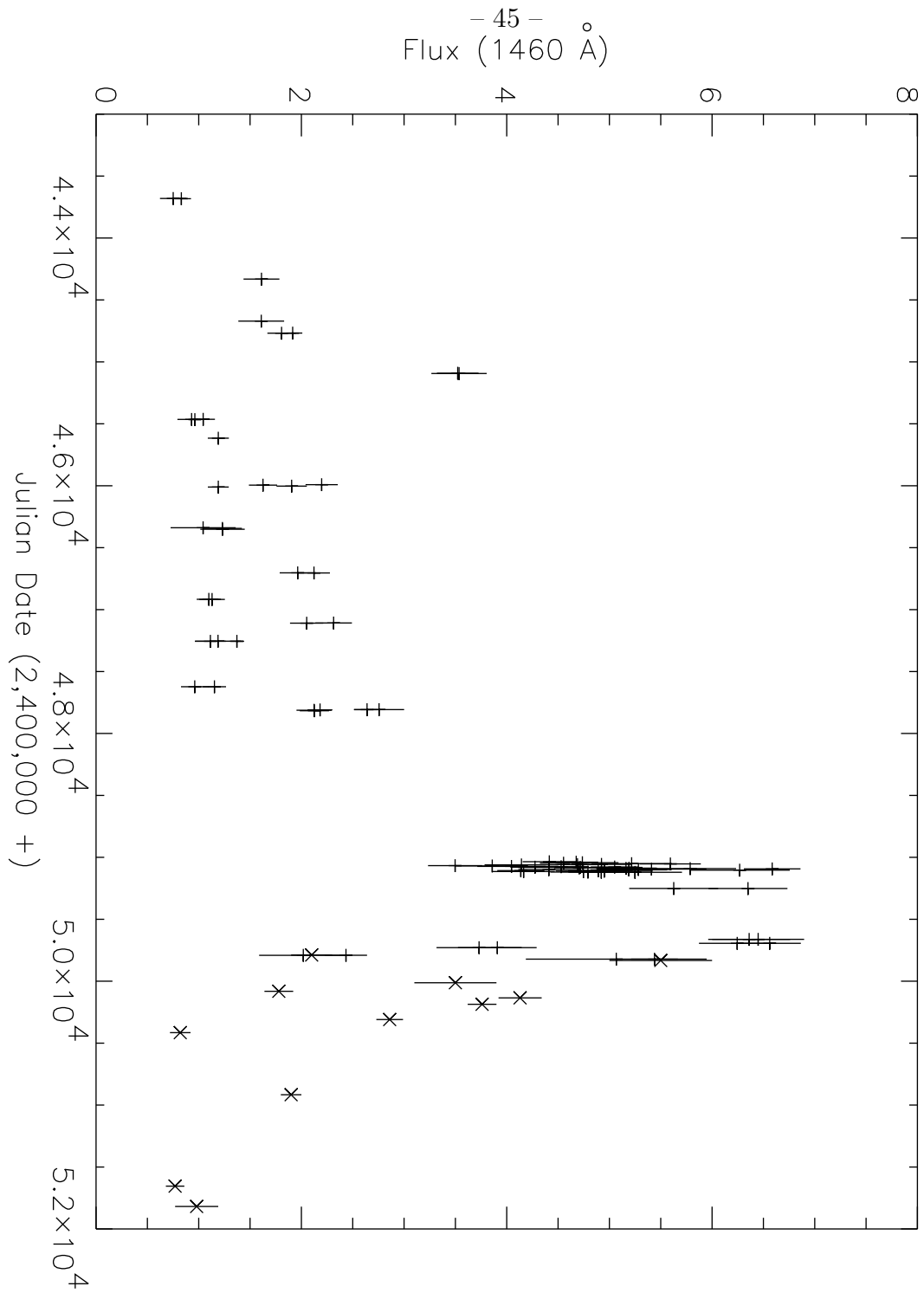


Fig. 3.

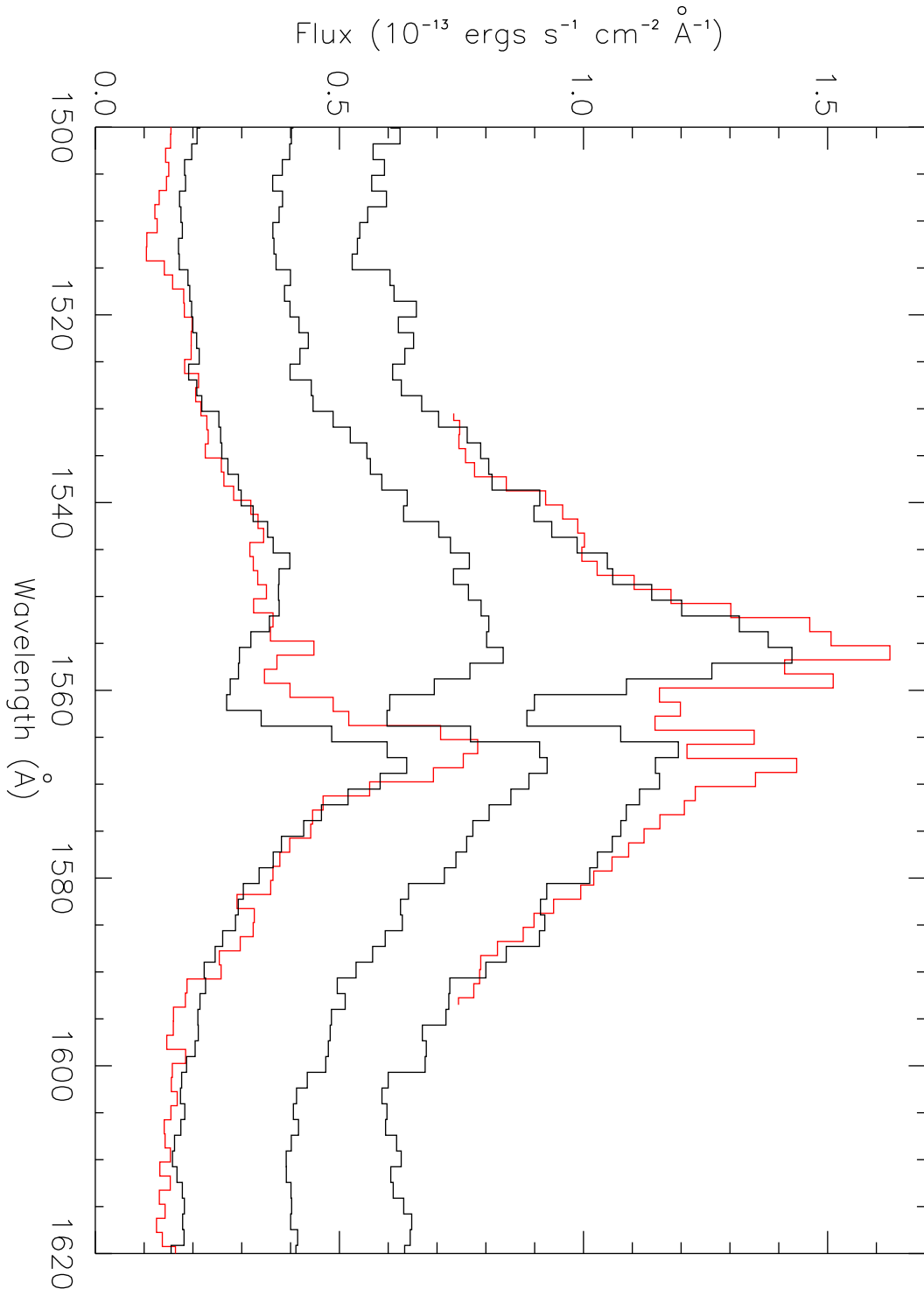


Fig. 4.

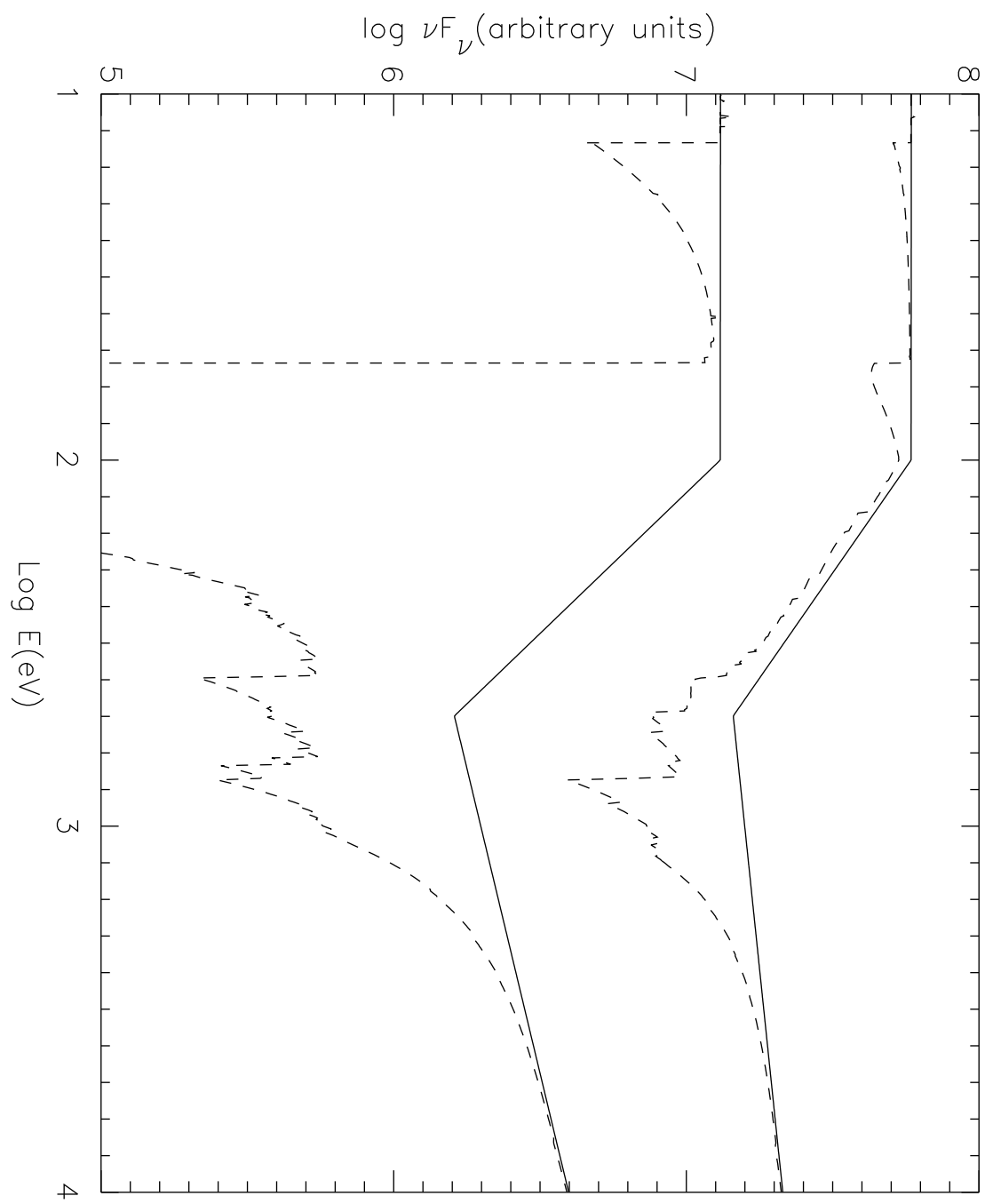


Fig. 5.

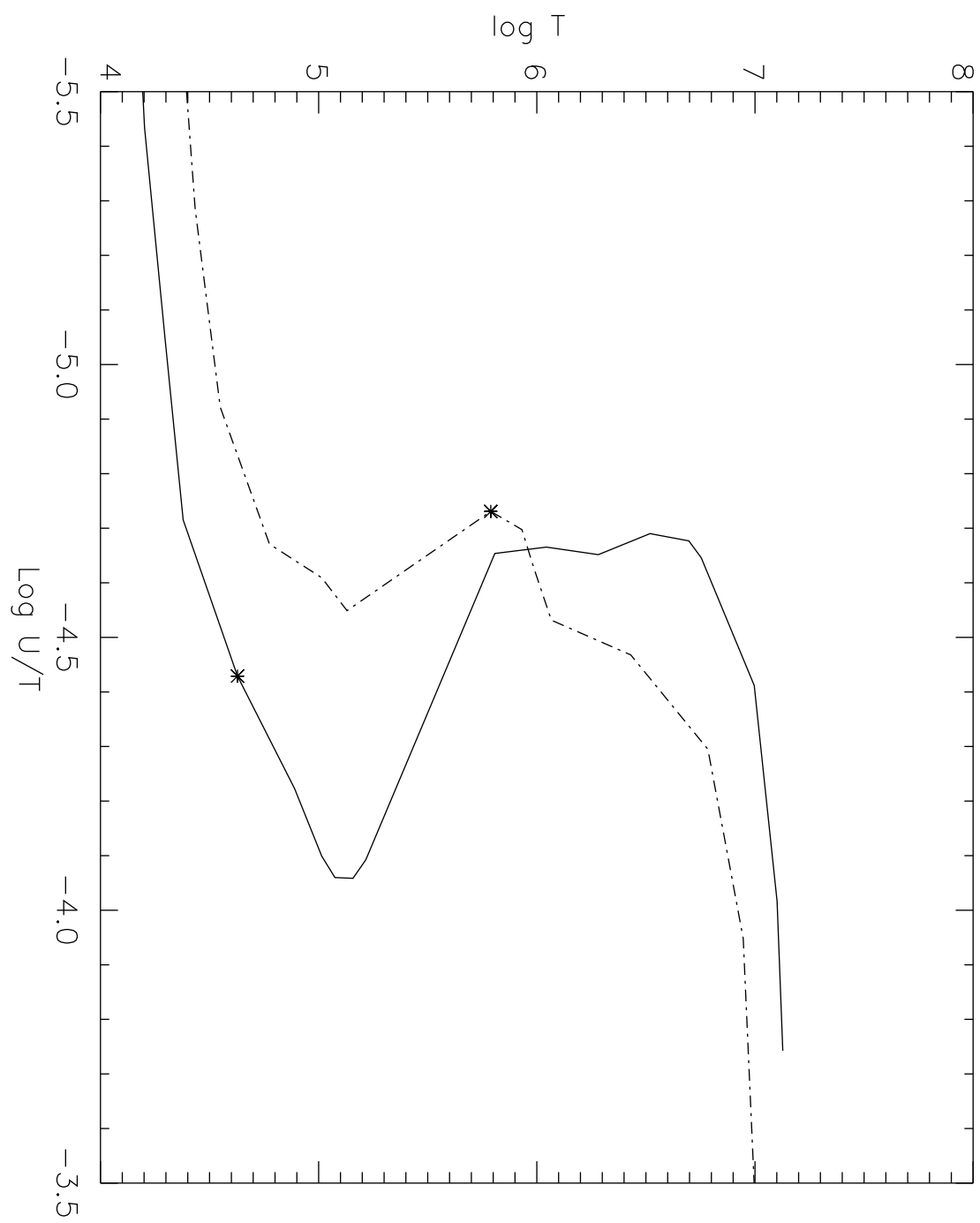


Fig. 7.

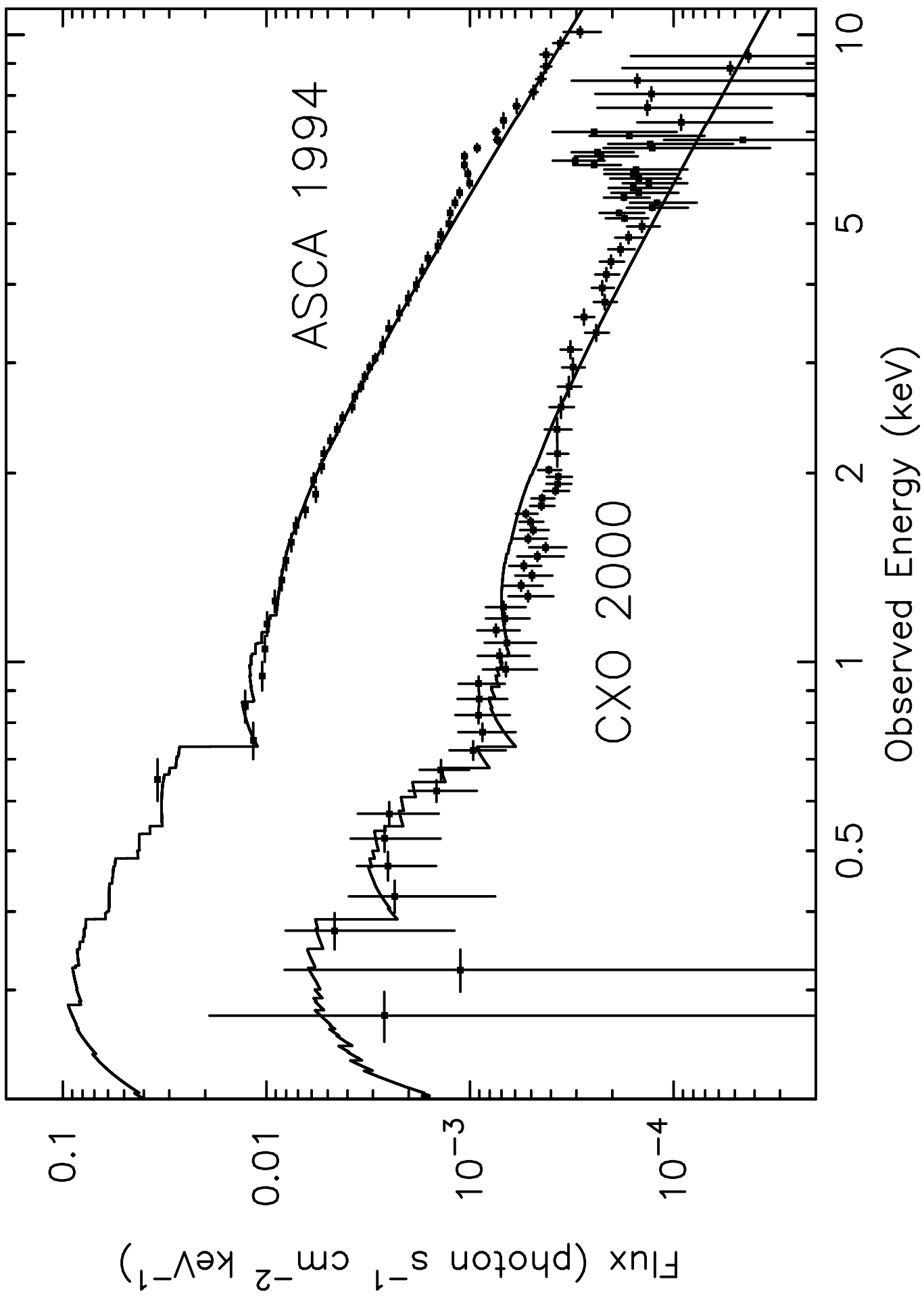


TABLE 7
COMPONENT 1A: PREDICTED IONIC COLUMN DENSITIES^a (IN UNITS OF CM⁻²)

| Element | I XI | II XII | III XIII | IV XIV | V XV | VI XVI | VII XVII | VIII XVIII | IX XIX | X XX |
|---------|----------|-----------|-------------|-----------|----------|-----------|-------------|---------------|-----------|----------|
| H | 7.52e+16 | 2.40e+21 | | | | | | | | |
| He | 1.04e+15 | 3.36e+19 | 2.07e+20 | | | | | | | |
| C | | 9.41e+12 | 9.43e+15 | 2.03e+17 | 5.50e+17 | 5.20e+16 | 9.77e+14 | | | |
| N | | 1.63e+12 | 3.42e+15 | 7.10e+16 | 6.85e+16 | 1.40e+17 | 5.28e+15 | 3.97e+13 | | |
| O | | 4.02e+13 | 1.22e+17 | 3.59e+17 | 4.94e+17 | 4.43e+17 | 2.11e+17 | 3.47e+15 | 1.63e+13 | |
| Ne | | 1.10e+13 | 2.46e+16 | 2.63e+16 | 1.11e+17 | 9.35e+16 | 7.02e+15 | 1.17e+15 | 1.67e+14 | 1.10e+12 |
| Mg | | 4.71e+12 | 3.38e+15 | 4.03e+15 | 5.87e+15 | 2.36e+16 | 2.87e+16 | 1.17e+16 | 1.69e+15 | 1.29e+14 |
| Si | 1.00e+13 | 3.60e+10 | 8.56e+12 | 1.96e+14 | 4.71e+15 | 1.86e+16 | 3.02e+16 | 1.72e+16 | 3.20e+15 | 2.74e+14 |
| S | 1.63e+13 | 6.48e+11 | 1.38e+13 | 4.92e+14 | 2.00e+15 | 6.09e+15 | 1.45e+16 | 9.98e+15 | 2.66e+15 | 2.71e+14 |
| Fe | 1.63e+13 | 7.54e+11 | 7.80e+09 | 1.24e+11 | 4.97e+14 | 1.68e+15 | 4.72e+15 | 1.56e+16 | 3.30e+16 | 2.88e+16 |
| | 2.13e+15 | 3.61e+14 | 5.03e+13 | 6.21e+12 | 9.19e+11 | 9.21e+10 | | | | |

^aModel Parameters: $U = 0.126$, $N_H = 2.4 \times 10^{21} \text{ cm}^{-2}$.

TABLE 8
 COMPONENT 1B: PREDICTED IONIC COLUMN DENSITIES^a (IN UNITS OF CM⁻²)

| Element | I | II | III | IV | V | VI | VII | VIII | IX | X |
|---------|----------|----------|----------|----------|----------|----------|----------|----------|----------|---|
| H | 3.06e+16 | 6.97e+18 | | | | | | | | |
| He | 1.95e+15 | 4.40e+17 | 2.58e17 | | | | | | | |
| C | 3.53e+11 | 2.23e+14 | 1.87e+15 | 2.72e+14 | 1.24e+13 | | | | | |
| N | 1.52e+11 | 6.31e+13 | 6.72e+14 | 1.02e+14 | 3.37e+12 | 4.39e+10 | | | | |
| O | 1.69e+12 | 4.15e+14 | 3.91e+15 | 4.10e+14 | 1.93e+13 | 1.56e+11 | | | | |
| Ne | 2.97e+10 | 2.85e+13 | 6.48e+14 | 8.86e+13 | 4.37e+12 | 3.24e+10 | | | | |
| Mg | 2.30e+10 | 1.36e+13 | 1.88e+14 | 2.82e+13 | 1.21e+12 | 2.01e+10 | | | | |
| Si | 4.26e+09 | 1.64e+13 | 1.46e+14 | 4.63e+13 | 8.25e+12 | 1.22e+11 | 9.17e+08 | | | |
| S | 4.55e+09 | 8.98e+12 | 7.55e+13 | 1.88e+13 | 1.46e+12 | 2.18e+11 | 1.73e+10 | | | |
| Fe | 2.38e+09 | 4.02e+11 | 3.21e+13 | 1.82e+14 | 5.40e+13 | 1.05e+13 | 6.21e+11 | 2.06e+10 | 6.38e+08 | |

^aModel Parameters: $U = 1.29\text{e-}03$, $N_H = 7.0 \times 10^{18} \text{ cm}^{-2}$.

TABLE 9
 COMPONENT 2: PREDICTED IONIC COLUMN DENSITIES^a (IN UNITS OF cm^{-2})

| Element | I XI | II XII | III XIII | IV XIV | V XV | VI XVI | VII XVII | VIII XVIII | IX XIX | X XX |
|---------|----------|-----------|-------------|-----------|----------|-----------|-------------|---------------|-----------|----------|
| H | 1.02e+17 | 3.90e+21 | | | | | | | | |
| He | 3.63e+13 | 1.81e+18 | 3.88e+20 | | | | | | | |
| C | | 1.12e+12 | 1.40e+15 | 5.22e+16 | 1.10e+18 | 1.67e+17 | 4.60e+15 | | | |
| N | | 7.59e+10 | 2.48e+14 | 1.03e+16 | 7.40e+16 | 3.64e+17 | 1.92e+16 | 2.10e+14 | | |
| O | | 1.79e+11 | 1.26e+15 | 6.15e+16 | 5.05e+17 | 1.06e+18 | 1.00e+18 | 2.22e+16 | 1.30e+14 | |
| Ne | | 2.47e+10 | 8.54e+13 | 5.63e+15 | 1.19e+17 | 2.58e+17 | 3.78e+16 | 6.89e+15 | 1.24e+15 | 8.66e+12 |
| Mg | | 9.50e+08 | 2.98e+12 | 1.65e+14 | 1.91e+15 | 2.35e+16 | 5.61e+16 | 3.85e+16 | 7.90e+15 | 6.25e+14 |
| | 4.75e+13 | | | | | | | | | |
| Si | | 1.55e+09 | 4.38e+11 | 1.96e+13 | 1.20e+15 | 1.39e+16 | 4.62e+16 | 4.54e+16 | 1.27e+16 | 1.38e+15 |
| | 8.40e+13 | 3.17e+12 | 1.24e+11 | | | | | | | |
| S | | 7.33e+08 | 6.67e+11 | 4.57e+13 | 4.54e+14 | 4.05e+15 | 2.01e+16 | 2.29e+16 | 9.40e+15 | 1.40e+15 |
| | 9.73e+13 | 4.54e+12 | 1.29e+11 | | | | | | | |
| Fe | | | | 6.25e+09 | 2.01e+12 | 2.03e+14 | 6.03e+15 | 3.82e+16 | 6.79e+16 | 3.18e+16 |
| | 9.60e+15 | 1.91e+15 | 2.85e+14 | 3.62e+13 | 5.09e+12 | 6.07e+11 | | | | |

^aModel Parameters: $U = 0.138$, $N_H = 3.9 \times 10^{21} \text{ cm}^{-2}$.

TABLE 10
 COMPONENT 3+4: PREDICTED IONIC COLUMN DENSITIES^a (IN UNITS OF CM⁻²)

| Element | I XI | II XII | III XIII | IV XIV | V XV | VI XVI | VII XVII | VIII XVIII | IX XIX | X XX |
|---------|----------|-----------|-------------|-----------|----------|-----------|-------------|---------------|-----------|----------|
| H | 2.87e+16 | 1.40e+21 | | | | | | | | |
| He | 4.87e+12 | 2.79e+17 | 1.40e+20 | | | | | | | |
| C | | 8.18e+10 | 1.05e+14 | 7.01e+15 | 3.50e+17 | 1.13e+17 | 5.90e+15 | | | |
| N | | 3.93e+09 | 1.26e+13 | 1.01e+15 | 1.42e+16 | 1.38e+17 | 1.42e+16 | 3.02e+14 | | |
| O | | 4.33e+09 | 2.84e+13 | 4.01e+15 | 6.77e+16 | 2.79e+17 | 5.76e+17 | 2.44e+16 | 2.49e+14 | |
| Ne | | 4.25e+08 | 2.76e+12 | 4.62e+14 | 1.97e+16 | 9.47e+16 | 2.87e+16 | 8.14e+15 | 2.22e+15 | 2.39e+13 |
| Mg | | | 3.18e+10 | 3.76e+12 | 9.22e+13 | 2.80e+15 | 1.44e+16 | 2.01e+16 | 7.72e+15 | 9.11e+14 |
| Si | 8.14e+13 | 2.84e+11 | 6.48e+09 | 3.38e+11 | 4.84e+13 | 1.34e+15 | 9.60e+15 | 1.96e+16 | 1.06e+16 | 2.03e+15 |
| S | 1.77e+14 | 8.08e+12 | 4.98e+11 | 1.15e+12 | 2.23e+13 | 3.44e+14 | 3.50e+15 | 8.26e+15 | 6.72e+15 | 1.92e+15 |
| Fe | 2.19e+14 | 1.41e+13 | 5.60e+11 | | | | | | | |
| | 1.77e+16 | 9.08e+15 | 2.81e+15 | 5.70e+14 | 9.40e+13 | 1.56e+13 | 2.19e+10 | 5.31e+12 | 3.44e+14 | 5.14e+15 |
| | | | | | | | 1.94e+12 | 2.50e+11 | | 2.02e+16 |

^aModel Parameters: $U = 0.185$, $N_H = 1.4 \times 10^{21} \text{ cm}^{-2}$.

TABLE 11
 COMPONENT 1A (HIGHSTATE): PREDICTED IONIC COLUMN DENSITIES^a (IN UNITS OF CM⁻²)

| Element | I XI | II XII | III XIII | IV XIV | V XV | VI XVI | VII XVII | VIII XVIII | IX XIX | X XX |
|---------|----------|-----------|-------------|-----------|----------|-----------|-------------|---------------|-----------|----------|
| H | 7.86e+15 | 2.40e+21 | | | | | | | | |
| He | 2.66e+11 | 8.48e+16 | 2.40e+20 | | | | | | | |
| C | | 5.40e+08 | 1.70e+12 | 4.58e+14 | 1.55e+17 | 4.61e+17 | 1.99e+17 | | | |
| N | | | 1.08e+11 | 3.22e+13 | 1.98e+15 | 1.46e+17 | 1.21e+17 | 1.87e+16 | | |
| O | | | 7.92e+10 | 5.02e+13 | 3.64e+15 | 6.85e+16 | 1.20e+18 | 3.34e+17 | 2.39e+16 | |
| Ne | | | 1.58e+09 | 1.59e+12 | 4.27e+14 | 1.57e+16 | 3.73e+16 | 6.71e+16 | 1.32e+17 | 1.14e+16 |
| Mg | 2.81e+14 | | | 4.28e+08 | 5.61e+10 | 1.36e+13 | 6.56e+14 | 8.60e+15 | 3.29e+16 | 2.65e+16 |
| Si | 1.02e+16 | 3.20e+14 | 2.99e+12 | | 9.15e+09 | 2.41e+12 | 1.69e+14 | 3.43e+15 | 1.78e+16 | 2.99e+16 |
| S | 1.86e+16 | 3.70e+15 | 7.30e+14 | | | | | | | |
| | | | | 1.55e+08 | 7.63e+09 | 2.61e+11 | 2.28e+13 | 5.67e+14 | 4.64e+15 | 1.25e+16 |
| Fe | 1.21e+16 | 5.14e+15 | 9.89e+14 | 1.07e+14 | 1.24e+13 | 6.86e+10 | | | | |
| | | | | | | 6.58e+08 | 3.22e+11 | 4.19e+13 | 1.56e+15 | 3.95e+15 |
| | 8.66e+15 | 2.21e+16 | 2.66e+16 | 1.83e+16 | 1.04e+16 | 2.85e+15 | 1.30e+15 | 9.32e+13 | 4.46e+12 | 1.79e+11 |

^aModel Parameters: $U = 0.79$, $N_H = 2.4 \times 10^{21} \text{ cm}^{-2}$.

TABLE 12
 COMPONENT 1B (HIGHSTATE): PREDICTED IONIC COLUMN DENSITIES^a (IN UNITS OF CM⁻²)

| Element | I | II | III | IV | V | VI | VII | VIII | IX | X |
|---------|----------|----------|----------|----------|----------|----------|----------|----------|----------|----------|
| H | 4.90e+15 | 7.00e+18 | | | | | | | | |
| He | 3.57e+13 | 4.48e+16 | 6.55e+17 | | | | | | | |
| C | 2.49e+09 | 8.21e+12 | 3.71e+14 | 9.37e+14 | 1.05e+15 | 1.01e+13 | 1.56e+10 | | | |
| N | 7.75e+08 | 1.95e+12 | 1.59e+14 | 4.02e+14 | 2.29e+14 | 4.86e+13 | 1.37e+11 | | | |
| O | 2.17e+09 | 5.11e+12 | 5.62e+14 | 2.39e+15 | 1.53e+15 | 2.58e+14 | 1.70e+13 | 1.68e+10 | | |
| Ne | 5.58e+07 | 3.34e+11 | 6.48e+13 | 2.90e+14 | 3.54e+14 | 6.06e+13 | 8.52e+11 | 3.74e+10 | | |
| Mg | 8.68e+07 | 1.01e+11 | 1.83e+13 | 7.46e+13 | 7.54e+13 | 5.44e+13 | 7.95e+12 | 3.59e+11 | 7.17e+09 | |
| Si | 2.93e+07 | 2.40e+11 | 1.01e+13 | 3.17e+13 | 9.78e+13 | 6.36e+13 | 1.26e+13 | 7.82e+11 | 1.63e+10 | |
| S | 2.12e+07 | 2.09e+11 | 9.98e+12 | 2.85e+13 | 2.70e+13 | 2.69e+13 | 1.15e+13 | 7.86e+11 | 2.10e+10 | |
| Fe | | 1.02e+07 | 8.63e+09 | 9.96e+11 | 1.68e+13 | 8.19e+13 | 1.23e+14 | 5.08e+13 | 6.18e+12 | 3.19e+11 |

^aModel Parameters: $U = 8.00e-03$, $N_H = 7.0 \times 10^{18} \text{ cm}^{-2}$.

TABLE 13
 COMPONENT 2 (HIGHSTATE): PREDICTED IONIC COLUMN DENSITIES^a (IN UNITS OF CM⁻²)

| Element | I XI | II XII | III XIII | IV XIV | V XV | VI XVI | VII XVII | VIII XVIII | IX XIX | X XX | |
|---------|----------|-----------|-------------|-----------|----------|-----------|-------------|---------------|-----------|----------|----------|
| H | 1.43+16 | 3.90e+21 | | | | | | | | | |
| He | 5.40e+11 | 1.51e+17 | 3.90e+20 | | | | | | | | |
| C | | 1.21e+09 | 3.61e+12 | 8.68e+14 | 2.50e+17 | 7.41e+17 | 3.35e+17 | | | | |
| N | | | 2.63e+11 | 7.10e+13 | 3.77e+15 | 2.30e+17 | 2.01e+17 | 3.37e+16 | | | |
| O | | | 2.16e+11 | 1.23e+14 | 7.77e+15 | 1.26e+17 | 1.88e+18 | 5.94e+17 | 4.57e+16 | | |
| Ne | | | 5.71e+09 | 4.93e+12 | 1.11e+15 | 3.42e+16 | 6.99e+16 | 1.12e+17 | 1.96e+17 | 1.62e+16 | |
| Mg | 3.63e+14 | | | | 1.51e+09 | 1.66e+11 | 3.42e+13 | 1.40e+15 | 1.60e+16 | 5.43e+16 | |
| Si | 4.16e+16 | 1.51e+16 | 4.10e+14 | 3.23e+12 | 2.68e+10 | 5.92e+12 | 3.54e+14 | 6.26e+15 | 2.96e+16 | 4.79e+16 | |
| S | 2.98e+16 | 5.91e+15 | 1.05e+15 | 1.10e+13 | 1.97e+10 | 6.23e+11 | 4.63e+13 | 1.01e+15 | 7.62e+15 | 2.00e+16 | |
| Fe | 1.95e+16 | 8.51e+15 | 1.64e+15 | 1.70e+14 | 1.77e+13 | 6.23e+10 | 2.13e+09 | 8.63+11 | 9.34e+13 | 2.95e+15 | 7.30e+15 |
| | 1.56e+16 | 3.66e+16 | 4.21e+16 | 2.88e+16 | 1.62e+16 | 4.49e+15 | 1.93e+15 | 1.28e+14 | 5.56e+12 | 1.58e+11 | |

^aModel Parameters: $U = 0.67$, $N_H = 3.9 \times 10^{21} \text{ cm}^{-2}$.

TABLE 14
 COMPONENT 3+4 (HIGHSTATE): PREDICTED IONIC COLUMN DENSITIES^a (IN UNITS OF CM⁻²)

| Element | I XI | II XII | III XIII | IV XIV | V XV | VI XVI | VII XVII | VIII XVIII | IX XIX | X XX |
|---------|----------|-----------|-------------|-----------|----------|-----------|-------------|---------------|-----------|----------|
| H | 3.83e+15 | 1.40e+21 | | | | | | | | |
| He | 1.43e+11 | 3.74e+16 | 1.40e+20 | | | | | | | |
| C | | | 3.29e+11 | 1.03e+14 | 4.71e+16 | 2.39e+17 | 1.90e+17 | | | |
| N | | | 2.67e+10 | 8.29e+12 | 5.91e+14 | 5.52e+16 | 8.60e+16 | 2.62e+16 | | |
| O | | | 2.27e+10 | 1.57e+13 | 1.15e+15 | 2.37e+16 | 5.49e+17 | 3.32e+17 | 4.57e+16 | |
| Ne | | | 3.27e+08 | 4.04e+11 | 1.19e+14 | 5.09e+15 | 1.45e+16 | 3.25e+16 | 8.90e+16 | 1.23e+16 |
| Mg | 4.43e+14 | | | 1.00e+08 | 1.43e+10 | 3.87e+12 | 2.37e+14 | 3.81e+15 | 1.57e+16 | 1.65e+16 |
| Si | 9.48e+15 | 3.95e+14 | 4.72e+12 | | 1.09e+09 | 3.76e+11 | 3.47e+13 | 9.26e+14 | 6.39e+15 | 1.55e+16 |
| S | 1.50e+16 | 4.44e+15 | 1.07e+15 | 1.67e+13 | 7.84e+10 | | | | | |
| | 7.59e+15 | 5.76e+15 | 1.82e+15 | 2.71e+14 | 3.57e+13 | 1.90e+10 | 2.23e+12 | 7.95e+13 | 9.91e+14 | 4.45e+15 |
| Fe | | | | | | 2.36e+11 | | | | |
| | 1.90e+15 | 7.62e+15 | 1.47e+16 | 1.37e+16 | 1.11e+16 | 3.05e+15 | 2.20e+15 | 2.26e+14 | 1.38e+13 | 6.84e+11 |

^aModel Parameters: $U = 0.845$, $N_H = 1.4 \times 10^{21} \text{ cm}^{-2}$.